

9 Metal to Non-metal Transitions in Solids and on Surfaces studied using Photoemission Spectroscopy

By K. E. SMITH

Department of Physics, Boston University, Boston, MA 02215, USA

1 Introduction

The scientific and technological interest in solid state resistivity transitions is enormous. The switching of the electrical properties of a material between those of a metal and those of a non-metal (be it semiconducting, semimetallic, insulating, or superconducting) is the very basis of the electronics industry. These transitions can be driven by numerous external and internal mechanisms, including, but not limited to, applied electric and magnetic fields, chemical doping, defects, pressure and temperature. While the technological applications of such transitions are myriad, these transitions are also the focus of significant fundamental physical and chemical interest. Indeed a substantial fraction of all research in solid state physics and chemistry is directed at understanding such transitions in some form or another, and almost every conceivable experimental technique has been applied in an attempt to identify their origin, and control their behaviour. Given that the transitions are primarily of interest owing to their effect on the electrical properties of solids, experimental techniques that probe electronic states are often the most useful in this endeavour.

In this paper I consider the application of photoemission spectroscopy to the study of selected metal to non-metal transitions. (The phrase 'metal to non-metal transition' is used in this paper to denote a generic resistivity transition between metallic and non-metallic states, and *vice versa*.) Photoemission is a very powerful technique that can provide direct information on the density of states, band dispersion and atomic bonding in solids.¹⁻⁴ Almost from its inception as a spectroscopic probe, photoemission has been used to study metal to non-metal transitions, and there have been a vast number of experiments reported. Rather than attempt to review this entire literature, I have chosen instead to select certain significant classes of metal to non-metal transitions and discuss the application of photoemission in their study. The most significant transition omitted here is the metal-superconductor transition. The application of photoemission in the study of superconductivity has been well reviewed elsewhere,⁵ and the field is so large that it would not be possible to discuss adequately the numerous other metal to non-metal transitions if superconductivity were included here.

The goal of this paper is to introduce the study of metal to non-metal transitions using photoemission spectroscopy to a general physics and chemistry audience.

Consequently I will describe the basic concepts of the spectroscopy itself, then discuss a series of case studies. Among the metal to non-metal transitions in solids that will be discussed here will be Mott–Hubbard transitions, Peierls transitions, and Verwey transitions. Furthermore, I will consider the relatively new field of metal to non-metal transitions at surfaces, where the transition occurs in the two-dimensional (2D) surface of a solid, rather than in the three-dimensional (3D) bulk. In this context, studies of the growth of metallic overlayers on surfaces, the modification of bulk transitions by surface adsorbates, and surface defect-induced transitions will be discussed.

The paper is structured as follows: in Section 2 various classes of metal to non-metal transitions will be briefly reviewed. Section 3 presents an introduction to photoemission spectroscopy. In this section three broad classes of photoemission experiments are identified, where the focus of each is the density of states, the band dispersion, or the core level electronic structure (bonding). The limitations and experimental constraints of photoemission spectroscopy will also be discussed. The main body of the paper is then divided into two primary sections: Section 4 will discuss photoemission studies of bulk metal to non-metal transitions, while Section 5 will consider transitions at surfaces. The paper concludes, in Section 6, with some thoughts about the future of such studies.

2 Metal to Non-metal Transitions—a Brief Review

There are numerous classes of metal to non-metal transitions, each with distinct origins. Some are driven by simple atomic geometric or proximity effects, others by chemical interactions, while yet others depend on subtle interactions between the vibrational and electronic structure.⁶ The theory underlying many of these transitions is well developed, but often an observed metal to non-metal transition will display characteristics of more than one type, complicating its classification. In this section the basic physics underlying a number of classes of metal to non-metal transitions will be briefly reviewed.

Wilson Transition

The most simple type of transition between metallic and non-metallic states is the so-called Wilson transition.⁶ Consider solids formed by the Group 2 elements (Be, Mg, *etc.*). The individual atoms have a closed s shell configuration, yet the solids themselves are metals. The explanation for the metallic nature of these solids is simple band hybridization. This is illustrated in Fig. 1, where the energy of the s and p states of a divalent atom are plotted against the interatomic distance. For large distances the s and p states are narrow localized levels, while at short distances they have hybridized due to band overlap to form s and p bands. Thus at large interatomic distances these solids should be insulators, while for short distances they should be metals. Such a transition in 3D bulk solids is difficult to study using photoemission spectroscopy, but can be probed for thin films on solid surfaces. An example of such studies will be discussed in Section 5.

Mott–Hubbard Transition

The original explanation provided by Mott for why solids with partially filled bands

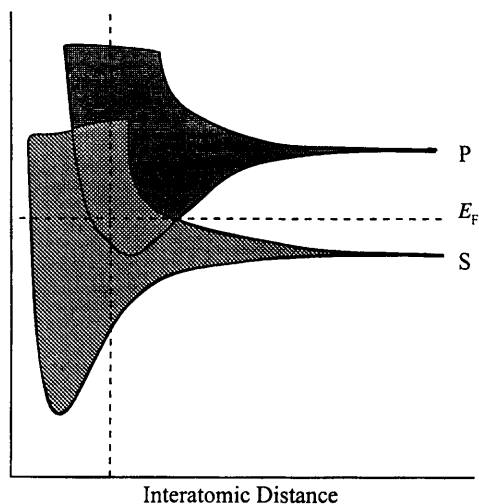


Fig. 1 Schematic illustration of the formation of a metallic band in the Wilson transition.

can be insulators depends on the concept of screening.⁶ (In a simple band picture, a material with a less than filled band should be a metal.) In the Thomas–Fermi approximation the potential-energy function for the electron is written

$$V(r) = - \left(\frac{ze^2}{r} \right) \exp(-\lambda r) \quad (1)$$

where $1/\lambda$ is the screening length, and $-ze^2/r$ is the unscreened Coulomb potential for an atom with z electrons. λ is given by

$$\lambda^2 \approx \frac{4me^2 n^{1/3}}{\hbar^2} \quad (2)$$

and is thus proportional to n , the density of electrons, and hence the density of atoms. Essentially, the unscreened Coulomb potential is reduced in magnitude by the screening term. If the potential of the ion cores is well screened, then there are no bound states for $V(r)$. If, however, the value of the screening term becomes close to unity, bound states can appear for the potential, localizing an electron around the ion. This will happen if λ becomes small, which occurs if the density of atoms is reduced. When the bound states appear in the potential, the material will have become an insulator. Thus a metal to non-metal transition can occur if the density of the metal is reduced. Note that this is a quite different mechanism than that of the Wilson transition, where it is the reduction in band hybridization that drives the transition. When the bound states appear in the potential, what were previously bands now become localized states. In the limit of an isolated atom, the gap that appears between the highest occupied level and the lowest unoccupied state is conceptually equal in magnitude to the difference between the ionization energy (occupied) and the electron affinity (unoccupied).

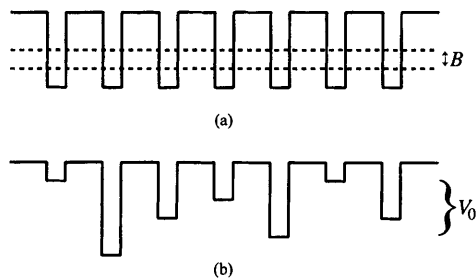


Fig. 2 A periodic array of potential wells. (a) Uniform well depth, with a bandwidth B ; (b) a random potential well depth within the limits $\pm V_0/2$.

The Mott–Hubbard transition includes in the model the intra-atomic Coulomb interaction for electrons on the same atom, where a material will become insulating if the intra-atomic Coulomb interaction (U) is larger than the bandwidth (W).^{6,7} The Mott–Hubbard picture of insulators is most often encountered in discussion of 3d transition metal compounds. These have partially filled 3d bands and should thus be metallic from a simple band perspective. That some are insulators is ascribed to $U > W$ effects. However, the Mott–Hubbard model fails to explain a very pronounced ligand effect in some transition metal compounds. A related model is that of the charge transfer insulator, which does adequately explain the ligand effect.⁸ Here the charge transfer energy (Δ) is taken into account, where Δ is the energy required to move an electron from a ligand sp state to a transition metal d state. If $\Delta > U$, then the interatomic Coulomb potential is the relevant parameter, and the material is a Mott–Hubbard insulator; if $\Delta < U$, then the material will be a charge transfer insulator.

Anderson Transition

The Anderson transition is a metal to non-metal transition associated with disorder in a solid.⁹ If the potential experienced by the conduction electrons in a solid contains a random component, their wavefunctions can localize and produce an insulating state. The model is illustrated in Fig. 2, which shows a periodic array of potential wells which are assumed to be far enough apart that the tight binding approximation is valid.^{6,9} Fig. 2(a) shows the case of a uniform well depth, and indicates a bandwidth B . Fig. 2(b) shows the same situation with a random potential well depth within the limits $\pm V_0/2$. According to Anderson, at a critical value of the ratio of the bandwidth to the random potential, $(V_0/B)_{\text{crit}}$, zero temperature diffusion of electrons is impossible, *i.e.*, the electrons have localized. When the temperature is raised above zero, current flows by thermally activated hopping. Similarly, electrons can localize when there is a set of uniform potential wells, but with random positions. The insulating state due to disorder is known as an Anderson insulator.

Mott observed that, even if the criterion for an Anderson insulator is not met, the states near the edges of a band are partially localized. He postulated that there exists a critical energy, E_c , that separates the localized from the non-localized states in a band. E_c is often referred to as the ‘mobility edge’, and for $E < E_c$ the conductivity is zero. Mott defines an Anderson transition as that resulting from the crossing of the Fermi

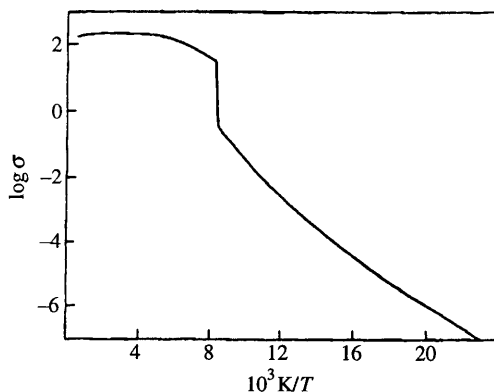


Fig. 3 Conductivity of Fe_3O_4 as a function of temperature.
(Reproduced with permission from *Rev. Mod. Phys.*, 1957, **29**, 279.)

level through E_c .⁶ As we shall see, such a transition can be achieved by changing the composition of a material.

Verwey Transition

A further type of metal to non-metal transition occurs in solids where the conduction electrons are in narrow bands for which atomic wavefunctions are good descriptions of the orbitals in a tight binding formalism.⁶ The narrow bands result in a large electron effective mass, which allows a form of Wigner crystallization of the electrons into an insulating state to occur. Wigner's hypothesis is that owing to mutual repulsion, a low density electron gas superimposed on a uniform positive background ('jellium') can crystallize into a non-conducting state if the potential energy due to the surrounding sphere of positive charge is greater than the zero point energy of the confined electron.¹⁰ The Verwey transition is a metal to non-metal, order-disorder transition observed as a function of decreasing temperature in certain narrow band solids where the number of electrons is smaller than the number of equivalent lattice sites. The narrow bandwidth is a consequence of the almost localized nature of the electrons, and reduces the kinetic energy term. At low temperatures the electrons can localize, owing to their mutual repulsion, into an ordered state, while at high temperatures the order is lost, and a conducting state appears.

The prototypical material that undergoes a Verwey transition is Fe_3O_4 , which exhibits a first order resistivity transition at $T_V = 120$ K. The low temperature state is insulating, and the resistivity decreases by two orders of magnitude when the crystals are heated through T_V . Surprisingly, above T_V the resistivity continues to decrease as the temperature is increased up to approximately 300 K, where a switch to a conventional metallic increase in resistivity with temperature is observed. This behaviour is plotted in Fig. 3.^{6,11} Verwey transitions are expected for transition metal oxides of mixed valence (such as Fe_3O_4), where polaron formation (strong electron-phonon coupling) leads to a large electron effective mass, and a low kinetic

energy. Fe_3O_4 has a room temperature inverse spinel structure which can be written as $\text{Fe}^{3+}(\text{Fe}^{2+}\text{Fe}^{3+})\text{O}_4$, with one third of the Fe ions located at tetrahedral 'A' sites as Fe^{3+} ions, and the remaining Fe ions equally distributed between so-called 'B2' and 'B3' sites as Fe^{2+} and Fe^{3+} ions, respectively. Below T_v , the B2 and B3 sites are indistinguishable, and in the orthorhombic low temperature phase, the Fe^{3+} and Fe^{2+} ions are ordered into alternate layers.⁶

While the existence of an ordered low temperature semiconducting phase is clear, the nature of the $T > T_v$ state is in some dispute, primarily owing to the observed decrease in resistivity with increasing temperature above T_v , despite the loss of long range order at T_v (Fig. 3). The issue is whether the Verwey transition is a metal to non-metal transition, or a non-metal to non-metal transition, *i.e.*, whether there is a true gap in the density of states both above and below T_v . As will be discussed in Section 4, photoemission spectroscopy has been applied to this problem by a number of groups, with contrasting results.

Peierls Transition

Peierls transitions are metal to non-metal transitions associated with low dimensional systems.¹²⁻¹⁴ They are observed frequently in quasi-1D solids, and there is strong evidence that they also exist in certain quasi-2D solids. (Indeed, as shall be seen, photoemission spectroscopy has played a large role in confirming this assertion). It is also postulated that they may exist on certain surfaces.¹⁵ Peierls transitions are the result of a very specific interaction between the electronic structure and the vibrational properties of 1D systems. In addition to a resistivity transition that occurs when the crystals are cooled, solids undergoing Peierls transitions also exhibit structural changes known as periodic lattice distortions (PLD), and modified electron density known as charge density waves (CDW). The change in the Brillouin zone associated with the PLD results in the formation of a gap in the electronic states at E_F and thus the occurrence of the resistivity transition. CDW are spatially inhomogeneous charge distributions that can move through the solid and provide additional mechanisms for current flow.

The Peierls transition is a result of the coupling of electronic states near E_F with collective vibrations of the lattice.^{16,17} Consequently, the behaviour of the electron-phonon interaction is crucial. When the electrons in a metallic system are perturbed by some periodic potential, the electrons move to screen the applied potential. A measure of this screening is provided by the generalized susceptibility, χ_q (where q is the wave vector associated with the periodic potential). χ_q is given by the expression

$$\chi_q = \sum_k \frac{f_k - f_{k+q}}{\varepsilon_{k+q} - \varepsilon_k} \quad (3)$$

f_k is the Fermi-Dirac function, and ε_k is the energy, for a state with wave vector k . $f_k - f_{k+q}$ is then the difference in the occupation number of two states separated by the wave vector q .² As is evident in eqn. (1), the susceptibility will become singular if $\varepsilon_k = \varepsilon_{k+q}$. This is precisely what occurs if $q = 2k_F$, where k_F is the Fermi wave vector of the Fermi surface. (When $q = 2k_F$, q is said to be a nesting vector of the Fermi surface.) The number of states coupled by the displacement vector $q = 2k_F$ is a function of the shape of the Fermi surface. Since in an ideal 1D metal the Fermi surface consists of two

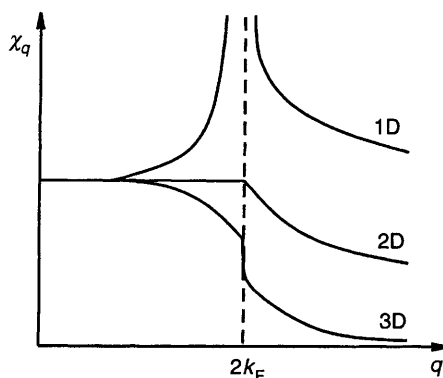


Fig. 4 Susceptibility as a function of displacement vector q . Note divergence at $q = 2k_F$.

parallel straight lines at $k = \pm k_F$, the displacement at $q = 2k_F$ couples all of the states at the Fermi surface, and the susceptibility diverges. This behaviour is illustrated in Fig. 4, which shows the divergence of χ in different dimensions.^{12,13} In general, the strength of the singularity depends on how heavily nested is the Fermi surface, *i.e.*, how many states are coupled by a specific nesting vector q .

The perturbing periodic potential (and thus the displacement vector q) can be associated with a phonon in the lattice. However, since the atom cores vibrating in the phonon mode are interacting *via* the screened Coulomb potential, it is clear that if $q = 2k_F$, then the screening will become singular and the frequency of the phonon mode falls at this wave vector. This is the origin of Kohn anomalies observed in the phonon dispersion curves for metals.¹⁷ In 1D and 2D systems, the singularity can be large enough to cause the frequency of the mode to fall to zero (a ‘giant Kohn anomaly’). If this occurs, a phonon is said to have frozen into the lattice, and the resulting distortion is the PLD.

Since the underlying lattice has distorted, the Brillouin zone must also distort, and the electron density $\rho(r)$ must change. The change in the electron density resulting from this coupling of the Fermi surface to the lattice vibrations is known as a charge density wave (CDW). When the Brillouin zone distorts to reflect the PLD, the band structure of the system must also distort. This distortion of the band structure can lead to a metal–insulator transition, the Peierls transition. This transition is illustrated in Figure 5. The figure shows an ideal 1D chain of atoms with period a . It is assumed to be in a normal metallic state, and has a half filled band. Thus $k_F = \pi/2a$. If the lattice vibrates such that $q = 2k_F$, then a PLD occurs, with period $2a$, a gap opens up at E_F in the electron density of states, and the system is in a CDW insulating state. (Note that a CDW/PLD state is destroyed at higher temperatures, owing in part to the broadening of the electron distribution at the Fermi level, which leads to a smaller anomaly in the generalized susceptibility.)

Peierls transitions also occur in quasi-2D materials with heavily nested Fermi surfaces. For example, CDW/PLD instabilities have been observed in the purple

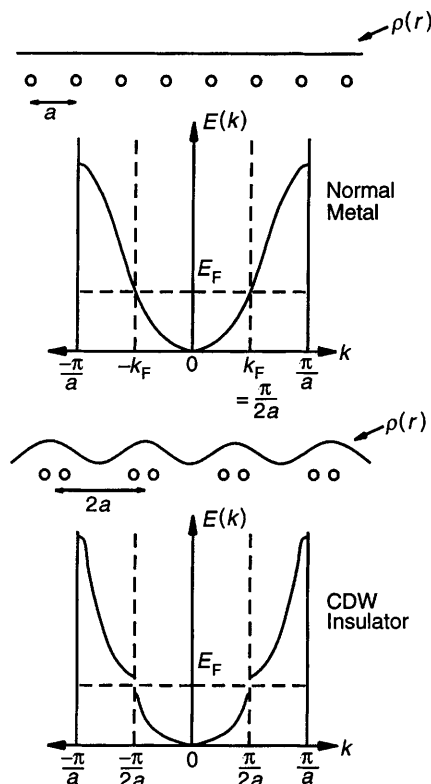


Fig. 5 Schematic illustration of the formation of a PLD and CDW during a Peierls transition in a 1D chain of atoms. See text for details.

molybdenum bronzes such as $\text{KMo}_6\text{O}_{17}$ and $\text{Na}_{0.9}\text{Mo}_6\text{O}_{17}$, in monophosphate tungsten bronzes of the form $(\text{PO}_2)_4(\text{WO}_3)_{2m}$, and in organic conducting salts such as $(\text{BEDT-TTF})_2\text{ReO}_4$ (where BEDT-TTF refers to bisethylenedithiotetrafulvalene).^{12–14} Many of these materials undergo a metal to metal transition (rather than a metal to non-metal transition) as a result of the opening up of a gap in only part of the Brillouin zone rather than the full zone. A concept known as hidden Fermi surface nesting was developed to explain the existence of CDW, PLD and Peierls transitions in both organic and inorganic quasi-2D conductors.^{18,19} Whangbo *et al.* introduced the idea that the Fermi surfaces in these materials can be viewed as a combination of quasi-1D structures, with distinct 1D nesting vectors.^{18,19} The essence of the idea is that the 2D Fermi surface would in fact be a simple combination of 1D (straight line) Fermi surfaces in the absence of avoided band crossing. These hidden 1D Fermi surfaces give the nesting vectors driving the Peierls transition.

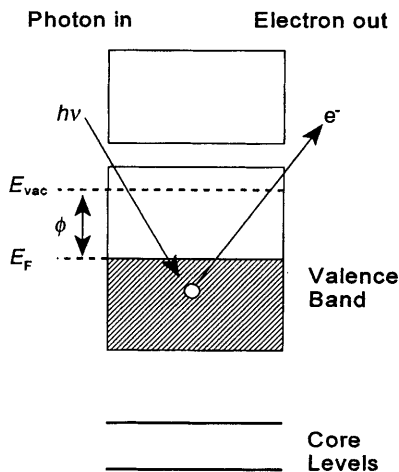


Fig. 6 Schematic of the photoemission process. E_F = Fermi level, E_{vac} = vacuum level, ϕ = work function.

3 Photoemission Spectroscopy—a Brief Introduction

Photoemission spectroscopy is a highly versatile probe of the electronic structure of solids and surfaces.^{1–4} In the photoemission experiment, a solid is exposed in vacuum to ultraviolet (UV) or X-ray radiation. The incident photons excite electrons from filled states below E_F to empty states above the vacuum level (E_{vac}), from where they can escape the solid. The basic photoemission process is illustrated in Fig. 6. In this section I will describe those concepts underlying the use of photoemission to measure solid state electronic structure that are relevant to the study of metal to non-metal transitions. There are numerous reviews of photoemission that focus in much more depth on the technique, and the curious reader is referred to these publications for a far more thorough discussion.^{1–4}

There are a number of variants of photoemission spectroscopy, each of which delivers somewhat different information. These variants are distinguished in practice by the energy of the incident photons and the mode of electron detection. Each variant has been used in the study of metal to non-metal transitions, and so will be discussed here. Also discussed in this section will be the experimental constraints associated with performing photoemission measurements, and a brief description of the equipment required.

Theory

General Considerations

The photoemission process can be viewed as one where a photon is destroyed, transferring its energy and momentum to the emitted electron. Energy conservation gives the Einstein relation for photoemission from a metal:

$$E_{K(\max)} = h\nu - \phi \quad (4)$$

where $E_{K(\max)}$ is the maximum kinetic energy for electrons emitted into vacuum, $h\nu$ is the photon energy, and ϕ is the work function of the surface. An electron that emerges with the maximum kinetic energy is the least tightly bound, and is thus emitted from a state at E_F . In general, the binding energy, E_B , of an electron in a solid can then be determined from the spectra by measuring the kinetic energy of the electron relative to that of an electron emitted from states at E_F . (Experimentally, the kinetic energy associated with states at E_F is determined for a given sample by having the sample in good electrical contact with a simple metal; the Fermi levels of the sample and the metal equalize, allowing the kinetic energy of electrons at E_F to be defined by using the metal rather than the sample. This is an important point, since as will be discussed in later sections, many conducting solids that undergo metal to non-metal transitions have very weak photoemission intensity at E_F .) Thus, using eqn. (4), E_B is given by:

$$E_B = E_{K(\max)} - E_K \quad (5)$$

where E_K is the kinetic energy of the electron measured in vacuum.

This analysis has thus far ignored the momentum of the electron, and the treatment of momentum distinguishes two of the variants of photoemission. Where both the momentum and the kinetic energy of the electron are measured, the spectroscopy is known as angle resolved photoemission (ARP). The name derives from the fact that measurement of the angle of emission of the electron in vacuum provides direct information on the k -vector (momentum) of the state in the solid. Where the kinetic energy is measured, integrated over a large number of emission directions (and hence integrated over momentum), the spectroscopy is known as angle integrated photoemission (AIP). A further distinction can be drawn by consideration of the energy of the photon used to excite the emission. States close to E_F are usually studied using low energy UV photons, while core states can only be excited by higher energy X-ray photons. The acronyms ARP and AIP will be reserved in this paper to describe photoemission spectroscopy performed with UV photons. [Indeed, AIP is often simply referred to as UV photoemission spectroscopy (UPS)]. Photoemission spectroscopy used in the study of core level electronic structure is customarily referred to as X-ray photoemission spectroscopy (XPS). XPS can be performed in either an angle integrated or an angle resolved mode. The information provided by each of these variants is quite different, as will be discussed below.

It is important to realize that photoemission spectroscopy is inherently surface sensitive. This is a direct consequence of the strong inelastic scattering (and resulting short mean free path) of low energy (5–1000 eV) electrons in solids.²⁰ Typical sampling depths are on the order of 5–10 Å. Consequently, if information on bulk electronic structure is sought, the surface of the solid has to be very well characterized. Great care has to be taken to prepare clean surfaces, and to avoid contamination of the surface during the measurement. These considerations necessitate that photoemission measurements be performed in an ultrahigh vacuum (UHV) environment. The inelastic scattering of electrons also leads to a background in all photoemission spectra due to the measurement of electrons that have lost energy or momentum prior to detection.

Angle Resolved Photoemission

ARP is a unique spectroscopy in that it can directly measure the dispersion of bands in

a solid.²⁻⁴ The 3D crystal momentum of the electron is conserved in the photoemission process:

$$\mathbf{k}_i = \mathbf{k}_f + \mathbf{G} \quad (6)$$

where \mathbf{k}_i and \mathbf{k}_f are the initial and final momenta of the electron and \mathbf{G} is a bulk reciprocal lattice vector. ARP measures, to a good approximation, \mathbf{k}_f , where the length of the vector is determined by the kinetic energy (which can be varied experimentally by varying the photon energy), and the direction is determined by the emission angle (which in practice is determined by varying the angle of detection). \mathbf{k}_i can then be determined to within a reciprocal lattice vector by eqn. (6).

The momentum vector can be resolved into two components, k_{\parallel} and k_{\perp} , parallel and perpendicular to the sample surface, respectively. The periodicity of an ideal infinite 3D crystal is broken by the surface, and when the electron leaves the crystal, absolute knowledge of k_{\perp} is lost. However, since the periodicity parallel to the surface is unchanged, k_{\parallel} remains a conserved quantity:

$$\mathbf{k}_{\parallel,i} = \mathbf{k}_{\parallel,f} + \mathbf{G}_{\parallel} \quad (7)$$

Thus ARP measurements of 2D states (either in layered materials or surface localized states) are the least ambiguous, since k_{\parallel} is the only good quantum number in these systems. Note that for emission normal to a surface, $k_{\parallel,f}$ is necessarily zero. For 2D systems, we can write

$$|\mathbf{k}_{\parallel}| = \sqrt{\frac{2mE_k}{\hbar^2}} \sin \theta \quad (8)$$

where θ is the angle of emission relative to the sample normal. Eqn. (8) immediately allows the band dispersion to be determined to within a surface reciprocal lattice vector.

For the purposes of studying metal to non-metal transitions, ARP can in principle be used to measure the changes in the band dispersion as the transition occurs. In the event of a transition that leads to a change in the Brillouin zone, the band dispersion will also change radically. A second, related, use of ARP in the area of metal to non-metal transitions is its ability to measure Fermi surfaces. A Fermi surface is measured using ARP in a very straightforward manner. The dispersion of a band is measured until the band crosses E_F , at which point the emission from the band should cease, since it is now unoccupied. The angle at which this occurs is converted into a momentum vector eqn. (8), thus giving one point of the Fermi surface. The full Fermi surface is then determined by measuring the dispersion of the band throughout the entire zone.

Angle Integrated Photoemission

The fundamental physics underlying angle integrated photoemission spectroscopy is identical to that just described above. The main difference between ARP and AIP lies in the mode of detection. In AIP, a spectrometer is used that simultaneously measures the kinetic energy of electrons emitted over a wide range of angles. This is in contrast to the ARP experiment, where the spectrometer is designed to measure the kinetic energy of electrons emitted only over as narrow a range of angles as possible. By measuring the electron kinetic energy over many angles simultaneously, the AIP spectrometer essentially integrates the photocurrent. Since the angle of emission is directly related to

the \mathbf{k} -vector of the electron state inside the solid [see eqn. (8)], the angular integration is thus over \mathbf{k} -vectors. Consequently, AIP measures the electronic density of states. (Strictly, the joint density of states.) The spectrometers needed for the experiments will be described below. The fundamental difference then between ARP and AIP is that ARP allows the determination of band dispersion, while AIP allows the measurement of the density of states.

The utility of AIP in the study of metal to non-metal transitions is clear. The changes in the density of states, and the formation of the energy gaps during the transition should all be accessible to measurement by AIP.

Intensity, Symmetry and Lifetime Effects

The relative intensities of photoemission features can be understood using Fermi's Golden Rule,²⁰ which expresses the photo-current $j(\mathbf{k})$ in terms of initial and final state wavefunctions (Ψ_i and Ψ_f) in the dipole approximation:

$$j(\mathbf{k}) = \left(\frac{e}{2mc} \right) \left(\frac{\hbar k}{8\pi^3} \right) \sum_i |\langle \Psi_f | \mathbf{A} \cdot \mathbf{P} | \Psi_i \rangle|^2 \delta(E_f - E_i - \hbar\nu) \quad (9)$$

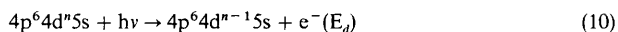
where \mathbf{A} is the vector potential of the incident light, and \mathbf{P} is the electronic momentum operator. The most important causes of relative intensity variations for the systems under consideration here are symmetry or polarization effects, and atomic or molecular cross-section variations. As regards symmetry effects, the matrix element in eqn. (9) can change dramatically if the orientation of the vector potential \mathbf{A} relative to the crystalline axes is varied.^{2-4,21-24} If photoelectrons are detected in a mirror symmetry plane, then the initial and final states must be either symmetric or anti-symmetric upon reflection. In an ARP experiment, the final state must always be symmetric, since if it were anti-symmetric, there would be a node located in the mirror plane and no photo-current could be detected. Consequently, the matrix element will be non-zero only if the product of the initial state symmetry and that of the vector potential is of even symmetry. This often allows the symmetry of the initial state to be determined, particularly in lighter elements where the impact of spin-orbit interactions is less pronounced. However, spin-orbit-induced hybridization often leads to 4d- and 5d-derived bands of mixed symmetry, which limits the utility of this effect. Atomic cross-section effects will be discussed below as resonant photoemission.

Note that photoemission spectroscopy measures the energy of an excited, quasi-particle state, and not the ground state. Thus, the binding energy plotted in photoemission spectra refers to the difference in energy between an N -particle ground state and an $N - 1$ -particle excited state. The band structure determined by ARP is thus more appropriately called a quasi-particle band structure, and it should be compared to ground state calculations with caution. However, the experimental bands have a direct relation to optical properties, while a first-principles calculated band structure does not. The intrinsic resolution is frequently determined by the lifetime of the final state hole and the photoelectron (approximately 10^{-14} – 10^{-15} s), resulting in an energy broadening on the order of 1 eV, which can be a significant limitation.^{25,26} However, spectral features near E_F are narrower due to the increased lifetime of the hole state (as predicted by Fermi liquid theory).²⁷ When dispersion curves are determined from ARP spectra, the impact of these lifetime effects is reduced since the

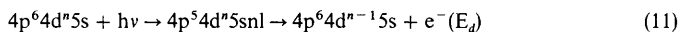
data points actually are determined by measuring the centroid of a particular spectral feature.

Resonant Photoemission

As mentioned above, a major influence on the relative strength of the photoemission yield are atomic effects. The most important such effect in the context of the study of metal to non-metal transitions is known as resonant photoemission.²⁸ The origin of this phenomenon is atomic autoionization, also called direct recombination. In this process a photon is absorbed and a core electron is excited into an unoccupied state above E_F . This state decays *via* an Auger process where the excited electron refills the core hole and a valence electron (usually) is excited out of the system. This process leaves the system in the same final state as direct photoemission. These two photoionization pathways add coherently, and lead to interference and resonant behaviour in the photoionization cross-section of the valence state as a function of photon energy. Hence the term resonant photoemission. This phenomenon can be illustrated by considering conventional and resonant photoemission from the 4d states in a transition metal compound. The ground state configuration can be written as $4d^n$, and conventional photoemission results in the formation of a $4d^{n-1}$ state with a hole in the d-band, and the emission of a d-electron into the vacuum with a kinetic energy E_d . This process can be written as:



However, if the photon energy is above the $4p \rightarrow 4d$ optical absorption edge, then resonant photoemission from the d-state can be written as:



where the electron is excited into a state designated nl , which is primarily 4d for this transition metal example. Thus a 4d electron is excited to an empty 4d which de-excites through an autoionization process where one 4d electron falls back to fill the 4p hole, transferring all of its energy to a second 4d electron which is emitted from the atom. Since the final state in eqn. (11) is identical to that arrived at by conventional photoemission in eqn. (10), it is clear that when the photon energy reaches the $4p \rightarrow 4d$ threshold, the number of electrons emitted with kinetic energy E_d increases. Thus in principle, resonant photoemission allows emission from particular states to be enhanced by tuning the photon energy, and allows the determination of orbital character in emission from hybrid states by measuring which features resonate at particular absorption thresholds.

X-Ray Photoemission Spectroscopy

There is one final, very important, variant of photoemission spectroscopy that must be discussed. We have seen that measurement of band dispersions requires angle resolved detection in order to measure the momentum of the photoemitted electron. Also, from consideration of cross-section effects and the size in k -space of Brillouin zones, ARP typically employs incident photons with energies in the 10–100 eV range. This is because the size of the zone in k -space converts to an angular spread of emitted electrons. However, eqn. (8) shows that if the kinetic energy increases, then higher angular resolution must be used to maintain the momentum resolution. Given a fixed

angular resolution, it then follows that if the kinetic energy increases, the momentum resolution decreases. At some point the emitted electrons detected in the cone of acceptance of even an ARP spectrometer will originate from throughout the zone, and hence an AIP experiment is being performed. The crossover from band to density of states effects as the dominant information contained in ARP spectra occurs below 100 eV. If much higher energy photons are used (100–1500 eV), then deep atomic core levels can be ionized. This is known as X-ray photoemission spectroscopy (XPS).¹ In principle, XPS measurements of core level binding energies allow the chemical state of atoms to be determined. There are many complicating features in the use of XPS to extract bonding information, but it has proved to be a very successful technique under appropriate conditions. It is important to note that valence band spectra can be measured in XPS. However, from the arguments presented above it is clear that such spectra will be momentum integrated and will exhibit quite different cross-section effects than those excited at lower energies.

XPS can often provide useful information on the changes in chemical bonding and atomic sites during metal to non-metal transitions. Furthermore, an important component in the line shape of XPS core level spectra are core-hole screening effects due to the electrons at E_F . As high energy electrons leave the solid they produce electron-hole pairs at E_F . Creation of these electron-hole pairs reduces the energy of the photoemitted electrons, which consequently appear to have higher binding energies. This leads to an asymmetrical lineshape for core level emission peaks from metallic samples, known as a Doniach-Sunjc lineshape.²⁹ When, or if, a material is insulating, the density of electrons at E_F is reduced and this asymmetry is likewise significantly reduced.

Experimental Considerations

To perform a photoemission experiment we require a monochromatic photon source, an electron kinetic energy analyser, and a suitable sample. As discussed above, an ARP spectrometer must be able to measure the kinetic energy of an electron emitted in a specific direction relative to the sample surface, while an AIP spectrometer has to be able to measure the kinetic energy of the electrons emitted over as wide a range of angles as possible. Photoemission spectrometers and vacuum ultraviolet radiation sources will be briefly described in this section; several reviews of these topics have been published and the reader is referred to these for more detailed information.^{20,30} A further topic that must be addressed when considering a real photoemission experiment is the sample. There are the significant constraints on the nature and quality of the solids that can be studied using photoemission techniques, and these will also be discussed below.

Photon Sources

There are three primary classes of photon sources used for photoemission spectroscopy: noble gas resonance lamps for UV sources, electron excited atomic de-excitation emission from solid targets for X-ray sources, and relativistic electron storage rings that emit synchrotron radiation in the UV and X-ray ranges. In the first of these, noble gases are excited by either a direct current discharge or microwave resonance, and the radiative de-excitation of the atoms provides several discrete photon energies between roughly 10 and 50 eV (depending on the gas used). For example, the primary emission

lines of an He discharge lamp lie at 21.2 eV (He I) and 40.8 eV (He II). Conventional X-ray sources used in XPS experiments consist of Al, Mg or other metal anodes onto which a high energy electron beam is directed. The electron beam ionizes atoms in the solid and the de-excitation of the system results in the emission of photons in the X-ray ranges. For an Al anode X-ray source, the energy of the primary emission is approximately 1486 eV. Both of these sources are quasi-monochromatic, in the sense that they emit discrete photon energies due to atomic transitions. The background (white) emission in X-ray sources can be significant, and for the UV sources there are multiple secondary lines visible in the emission spectrum. The third class of sources are synchrotrons. In contrast to unpolarized resonance lamps and X-ray tubes, electron storage rings provide a linearly polarized (in the plane of the ring), white-light source of radiation from the infrared to the hard X-ray. By the use of suitable monochromators, any photon energy in this range can be obtained. The tunability and linearly polarized nature of synchrotron radiation has made synchrotrons the source of choice for modern photoemission experiments, since all the symmetry and resonance effects discussed above are accessible.

Electron Spectrometers

Numerous electron spectrometer designs are used in photoemission experiments. The most common type are spherical deflection analysers (SDA) coupled to cylindrical element electron lenses to image photoelectrons from the sample onto the entrance plane of the analyser.^{2,20,30,31} Such designs are intrinsically angle resolving and provide fairly good energy resolution with only moderate overall dimensions. Only one angle is measured at a time, and ARP spectra are recorded individually by positioning the analyser at a particular angle relative to the sample. This means that the analyser has to be moved inside the vacuum chamber. By adjustment of the lens elements on an SDA design, this type of spectrometer can also be used in a pseudo-angle integrating mode. As discussed above, at higher photon energies, the kinetic energy will be large enough that band effects will be minimal, even with an SDA. AIP experiments are often performed using double-pass cylindrical mirror analysers (CMA), which collect electrons emitted in a wide annulus off the surface.^{29,30} A class of spectrometer that can be used for both ARP and AIP is known as the 2D display analyser. These collect the electrons emitted over a full cone from the surface.^{2,20,30}

Samples

There are numerous constraints placed on the size and nature of the samples that can be studied using photoemission spectroscopy. These constraints are interrelated. The first is the need for large samples. Continued improvements in SDA lens designs and focussed X-ray optics are alleviating this problem, but in general samples of the order of 1 to 3 mm² are required for routine photoemission measurements. If powdered samples are used this is not a serious limitation, but photoemission studies of powdered compounds are problematic for another reason, namely the need for well characterized surfaces. As discussed earlier, photoemission is an intrinsically surface sensitive spectroscopy. Thus sample surfaces have to be atomically clean and have to remain so during the course of the experiment. Attaining clean surfaces of powders is often very difficult, and the surfaces are ill-defined. Furthermore, if ARP experiments are to be undertaken, the surfaces also need to be well ordered. Clean, ordered surfaces can be

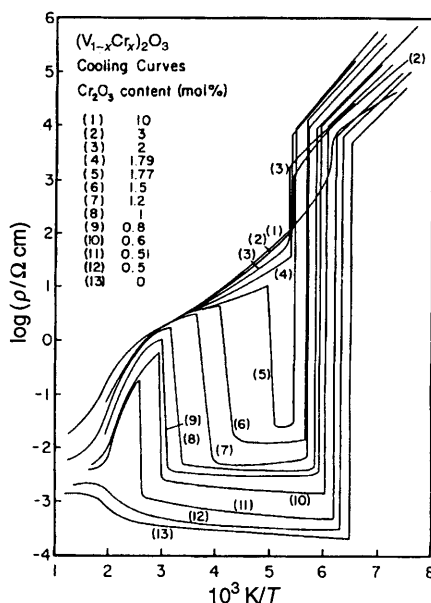


Fig. 7 Variation of resistivity with temperature for Cr-doped V_2O_3 .
(Reproduced with permission from *Phys. Rev. B*, 1980, **22**, 2626.)

obtained by cleaving the sample in UHV to expose a fresh plane of the crystal, by growing the sample *in situ*, or by atomically cleaning a surface by ion bombardment followed by heat annealing (to reduce the disorder resulting from the bombardment). In the case of cleaving or sputter/annealing, it is understood that the samples in this case are single crystals to begin with, and thus these crystals have to satisfy the described size constraint.

4 Metal to Non-metal Transitions in Solids

In this section photoemission studies of selected bulk metal to non-metal transitions will be reviewed. As mentioned earlier, there are a large number of such studies, and only a very few can be discussed here. However, the applicability and power of photoemission spectroscopy in the study of such transitions should become evident from the examples presented here.

Composition and Temperature Induced Transitions in Cr-doped V_2O_3

The first example of the application of photoemission in the study of metal to non-metal transitions concerns the transition metal oxide V_2O_3 .³² Pure and Cr-doped V_2O_3 exhibit dramatic metal to non-metal transitions, as indicated in the resistivity *versus* temperature plot presented in Fig. 7.³³ Pure V_2O_3 goes through two transitions

as a function of temperature: a first-order transition at 150 K from a monoclinic antiferromagnetic insulator at low temperatures to a trigonal metallic state, and a broad (≈ 150 K) second-order transition from this metallic state to a semiconducting one at 450–500 K.³⁴ When doped with Cr, additional transitions occur. First, the metallic state becomes progressively more insulating at a fixed temperature with the addition of Cr, the resistivity rising by an order of magnitude for each at.% Cr incorporated into the crystal.³³ Second, a new transition is observed as the temperature is increased above 170 K,^{33,35} the trigonal metallic state is observed to revert to an insulating state, but with no change in crystal symmetry. The temperature at which this transition occurs is a function of the Cr concentration. (This transition from the metallic to the insulating state with increasing temperature will be referred to here as the high-temperature transition; the transition from an antiferromagnetic insulator to a metallic state at approximately 150–170 K, which also occurs in pure V_2O_3 , is referred to here as the low-temperature transition.) The mechanisms underlying these transitions are the subject of much controversy,³³ but all are related to the concept of a Mott insulator.⁶ As discussed in Section 2, Hubbard introduced U/W as the relevant parameter for the problem, where U is the intra-atomic Coulomb energy and W is the one-electron bandwidth.⁷ Typically, when $U/W < 1$ a rigid band picture is a valid description of the electronic structure, whereas if $U/W > 1$ a highly correlated electron gas picture is usually more valid; in V_2O_3 , $U/W \approx 1$. Consequently, a variety of physical mechanisms have been proposed to explain the transitions in Cr-doped V_2O_3 , particularly the high-temperature transition, and many rely on the Mott-Hubbard concept. A thermodynamic theory by Spalek *et al.* based on Fermi liquid theory, and consisting of bands narrowed by correlations transforming into a lattice of localized spins, predicts many of the features of the Cr-doped V_2O_3 phase diagram.³⁶ Park *et al.* have proposed a model based on Anderson localization with strong hybridization between the V 3d and O 2p bands.³⁷ This model leads to a greatly reduced U .

Both pure and Cr-doped V_2O_3 have the corundum structure, with Cr entering the lattice substitutionally.³⁴ V_2O_3 is easily studied using photoemission techniques since large single crystals can be grown, and they cleave to expose well ordered (10 $\bar{1}$ 2) surfaces. The unit cell consists of a ten-atom basis made up of two M_2O_3 molecular units. While the electronic structure for single crystals of pure V_2O_3 has been studied by a number of groups using photoemission spectroscopy,^{37–43} the focus here will be studies of the changes in electronic structure during the metal to non-metal transitions. The spectra discussed here were obtained with a He I resonance lamp ($h\nu = 21.2$ eV), an Al-anode X-ray source ($h\nu = 1486$ eV), and using synchrotron radiation. All spectra were recorded in an angle integrated mode with a CMA. The resolution for the valence band spectra was 250 meV, while for the core level spectra the resolution was approximately 800 meV. Since the valence band spectra were recorded in an angle integrated mode, the spectra can be related directly to the density of states, and the presence of an energy gap should be clearly visible.

Composition Induced Transitions

V_2O_3 doped with either 1.5 or 3 at.% Cr is insulating at room temperature, with resistivities three to four orders of magnitude larger than that of pure V_2O_3 , which is metallic at this temperature. Thus the incorporation of Cr into the lattice induces a metal–insulator transition at room temperature in V_2O_3 . Fig. 8 shows the angle

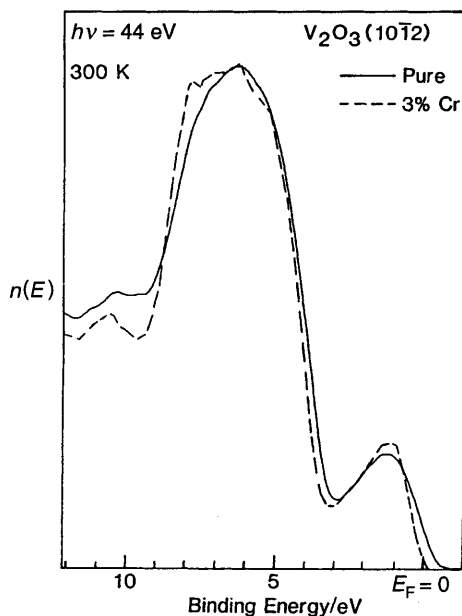


Fig. 8 Room temperature AIP spectra for pure and 3 at.% Cr-doped $V_2O_3(10\bar{1}2)$, taken with $h\nu = 44$ eV.

(Reproduced with permission from *Phys. Rev. B*, 1994, **50**, 1382.)

integrated photoemission spectra obtained from both pure and Cr-doped $V_2O_3(10\bar{1}2)$ (3 at.% Cr) single-crystal surfaces using synchrotron radiation ($h\nu = 44$ eV).³² A dramatic shift of the V 3d emission away from E_F , and the opening of a gap, is clearly visible in the spectra from the 3 at.% Cr-doped V_2O_3 . This is consistent with the bulk resistivity data of Fig. 7. In the theory of Spalek *et al.*, the effective Hubbard parameter U/W increases linearly with Cr content, with both an increase in U and a decrease in W .³⁶ At the critical value of $U/W = 1.646$, a discontinuous transition from a metallic to an insulating phase is predicted. The spectra of Fig. 8 indicate that, as Cr is added to V_2O_3 , the V 3d emission not only moves away from E_F , but narrows as well. The width of the V 3d emission above a straight line background decreases by approximately 0.3 eV when the spectrum from pure V_2O_3 is compared with one from a crystal doped with 3 at.% Cr. This direct observation of a narrowing in the V 3d density of states is consistent with the model described above.³⁶ Dramatic changes in the core-level spectra during this composition induced transition are also observed and will be discussed below, together with the similar changes observed during the temperature induced transition.

Fig. 9 shows the O 1s and V 2p core-level XPS spectra from pure and 1.5 at.% Cr-doped $V_2O_3(10\bar{1}2)$ at room temperature. The V 2p emission is a multiplet split into V 2p_{1/2} and V 2p_{3/2} peaks. For illustrative purposes only, the V 2p peaks were deconvoluted into the minimum number of Gaussians which would adequately fit the spectra (above a straight line background). For pure V_2O_3 [Fig. 9(b)], it was found

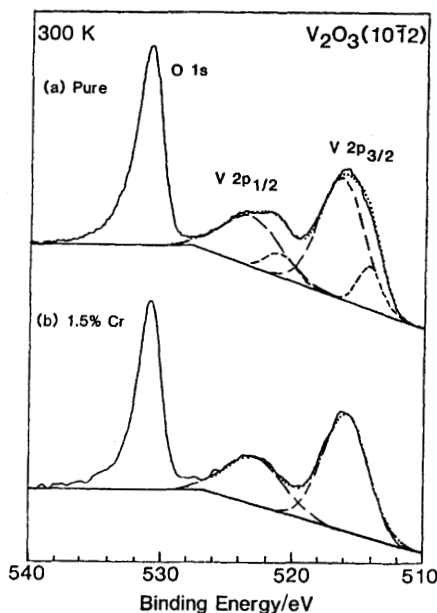


Fig. 9 O 1s and V 2p spectra from room temperature ($10\bar{1}2$) surfaces. (a) Pure V_2O_3 ,⁴⁴ (b) V_2O_3 doped with 1.5 at.% Cr. $h\nu$ 1486.6 eV.³² (Reproduced with permission from *Phys. Rev. B*, 1983, **28**, 6699 and 1994, **50**, 1382.)

that the V $2p_{1/2}$, $2p_{3/2}$ emission features could only be satisfactorily deconvoluted by two pairs of Gaussians.⁴⁴ However, the V 2p emission from 1.5 at.% Cr-doped V_2O_3 can be satisfactorily reproduced by using only one pair of Gaussian peaks; this is shown in Fig. 9(a). These Gaussians are almost identical to the major pair of Gaussians used in the pure V_2O_3 deconvolution, but they are shifted to lower binding energy by 0.6 eV. Note also that there exists an asymmetry on the high binding energy side of the O 1s emission from pure V_2O_3 [Fig. 9(b)]; this asymmetry is significantly reduced for the Cr-doped V_2O_3 spectrum. The origins of the significant changes in lineshape of both cation and anion core-level emission from V_2O_3 when doped with Cr will be discussed below.

Temperature Induced Transitions

Fig. 7 indicates that at room temperature a 1.5 at.% Cr-doped V_2O_3 crystal is insulating, and has nearly the same resistivity as one doped with 3 at.% Cr. The spectra from 1.5 and 3 at.% Cr-doped samples were found to be essentially identical at room temperature; the 3% Cr spectrum is shown in Fig. 8. As the 1.5 at.% Cr- V_2O_3 crystal is cooled below room temperature, it experiences two transitions (Fig. 7). At approximately 240 K the resistivity drops by almost three orders of magnitude and the sample becomes metallic; note, however, that the resistivity in this state is still almost two orders of magnitude larger than that of the metallic state in pure V_2O_3 . Further cooling of the crystal causes the resistivity to rise again; at approximately 170 K the sample

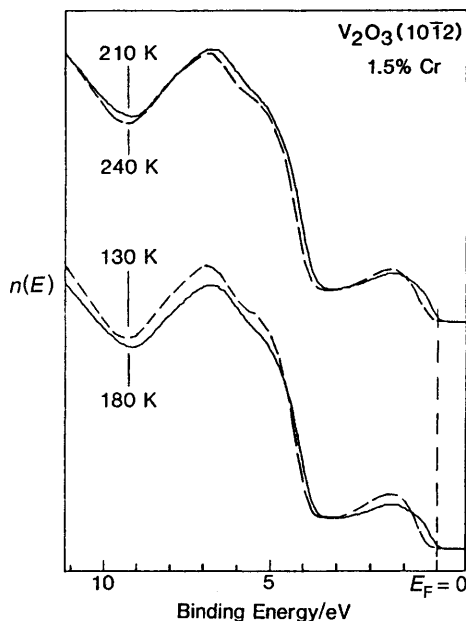


Fig. 10 UPS spectra from cleaved 1.5 at.% Cr-doped $V_2O_3(10\bar{1}2)$ cooled to 240, 210, 180 and 130 K. $h\nu = 21.2$ eV.

(Reproduced with permission from *Phys. Rev. B*, 1994, **50**, 1382.)

returns to an insulating state, with a six order of magnitude change in resistivity from the metallic state. Note that the resistivity of this low-temperature insulating state is more than a thousand times larger than that of the room temperature insulating state.

Figure 10 presents the photoemission spectra from 1.5 at.% Cr- V_2O_3 as the crystal is cooled below room temperature. The spectrum taken with the crystal at 240 K is similar to the room temperature spectrum, with very low emission intensity at E_F . Upon cooling the sample to 210 K, the spectrum changes dramatically, with the V 3d states shifting towards E_F . Further cooling to 180 K does not result in any significant change in the spectrum. However, when the crystal is cooled to 130 K, the V 3d emission moves away from E_F and a gap in the emission is seen to open up at E_F . Note that the metallic phase exhibits a smaller emission intensity at E_F than does pure V_2O_3 at room temperature (Fig. 8). This is consistent with the observation that the resistivity in the metallic phase of 1.5 at.% Cr-doped V_2O_3 is almost one hundred times that of pure metallic V_2O_3 (Fig. 7), and the assertion by Kuwamoto *et al.* that even in the metallic phase the density of electrons at E_F must be extremely low.³³ The origins of this high-temperature first-order transition are quite complex and are the subject of much controversy; eight distinct mechanisms are listed in ref. 33. A common feature of many of these theories is a narrowing of the V 3d bands in the insulating phase. Analysis of the data in Fig. 10 reveals that the V 3d emission in the room temperature insulating state is 0.15 eV narrower than that in the metallic state

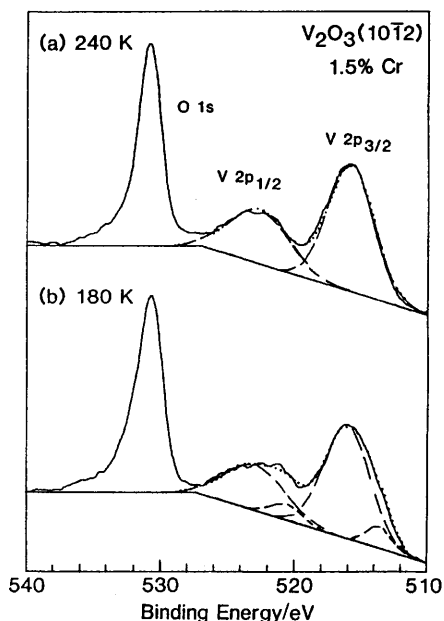


Fig. 11 O 1s and V 2p XPS spectra from cleaved 1.5 at.% Cr-doped $V_2O_3(10\bar{1}2)$ surfaces at (a) 240 K and (b) 180 K. $h\nu = 1486.6$ eV. (Reproduced with permission from *Phys. Rev. B*, 1994, **50**, 1382.)

at 210 K. This observation is consistent with the above theories, and the fact that the V 3d emission is consequently 0.15 eV narrower in the metallic state of Cr-doped V_2O_3 than the metallic state of pure V_2O_3 is consistent with the higher resistivity of the 210 K Cr-doped V_2O_3 metallic state.

When cooled further to 130 K, the spectra of Fig. 10 show that the material reverts to an insulating state. The spectra reveal that the density of states at E_F is considerably smaller at 130 K than at 180 K. As with the high-temperature transition, the V 3d emission narrows as the material becomes more insulating. The symmetry of the lattice changes during this transition, going from trigonal in the metallic to monoclinic in the insulating state.³⁴ Additionally, the volume increases by up to 3.5% at the low-temperature transition.³⁴ The mechanism driving this transition (which also occurs in pure V_2O_3) is different from that driving the high-temperature transition. Specifically, the low-temperature transition is driven by the Coulomb interaction between vanadium d-electrons, which results in an antiferromagnetic arrangement of relatively localized spins.³³ (The low-temperature insulating phase is antiferromagnetic, while the metallic phase is paramagnetic.) Again, the observed narrowing of the V 3d emission and opening up of a gap at E_F are consistent with theory.^{33,36}

The O 1s and V 2p XPS spectra for this sample in both the insulating phase at 240 K and the metallic phase at 180 K are shown in Fig. 11(a) and (b), respectively. The

spectrum obtained from the 240 K insulating sample is similar to the room temperature spectrum of Fig. 9(a), and can be reproduced by using only one pair of Gaussians. The separation of these Gaussians and their FWHM and relative intensities are identical to the Gaussians required to fit the room temperature spectrum. When the crystal goes through the high-temperature transition and becomes metallic, the V 2p core-level spectra change dramatically. The O 1s and V 2p spectra from a crystal at 180 K are shown in Fig. 11(b). It is clear in this figure that two pairs of Gaussians are now required to fit the spectrum adequately. As mentioned above, further cooling the sample to 130 K results in an O 1s/V 2p spectrum very similar to the 240 K spectrum of Fig. 11(a). Thus, in both the low- and high-temperature insulating phases, only one pair of Gaussians is required to fit the V 2p spectrum, while two pairs are required in the metallic phase (as for pure V_2O_3). Note also that the O 1s line in Fig. 11 becomes more asymmetrical in the metallic phase.

Changes in Core-level Emission during Metal to Non-metal Transitions

As just described, when Cr-doped V_2O_3 is in an insulating state, either at room temperature or at 130 K, the V 2p doublet is adequately described by a single pair of Gaussian peaks. This is in sharp contrast to the situation in metallic V_2O_3 at room temperature, or metallic Cr-doped V_2O_3 at 210 K, where two pairs of Gaussian peaks are required to fit the V 2p doublet. This extra doublet in the metallic phase is a screening effect: *i.e.*, the changes in the V 2p spectra are not related to chemical shifts of the V 2p level, but rather are related to the photoemission process itself. A variety of screening phenomena can occur in transition-metal oxides during photoemission. Even in the absence of a significant electron density near E_F , core holes are to some extent screened by the electrons in the solid.⁴⁵⁻⁴⁷ Thus when Cr-doped V_2O_3 is insulating at room temperature and has few electrons at E_F , the resulting V 2p binding energies are characteristic of poorly screened emission rather than unscreened emission. When the crystal becomes metallic at 210 K, there are many more electrons at E_F with which to screen the core hole, and metallic screening occurs. Thus, the small pair of Gaussians which are seen in the deconvolution of the V 2p doublet in the metallic state are associated with well screened emission from the V 2p levels and the large pair with the poorly screened emission. The ability to turn on and off metallic screening by taking this material through a metal-insulator transition allows unambiguous identification of the effects of such screening.

The O 1s emission also changes shape as a metal-insulator transition occurs. In metallic V_2O_3 and Cr-doped V_2O_3 the O 1s line has a large asymmetry on the high binding energy side of the peak (Fig. 9 and 11). This is a Doniach-Sunjc lineshape as discussed earlier. Clearly, as the solid becomes insulating and the density of electrons at E_F falls, the asymmetry is significantly reduced (Fig. 9 and 11). The correlation between changes in core level metallic screening and the observation of metal to non-metal transitions will be encountered again in this chapter.

In many ways the Cr-doped V_2O_3 system provided a 'text book' introduction to the study of metal to non-metal transitions using photoemission spectroscopy. The changes in the valence band density of states and the core level screening were easily observed, and there were no sample-related problems. The next example we will consider also concerns a transition metal oxide system, but in this case an Anderson transition will be examined.

Composition Induced Transitions in Sodium Tungsten Bronzes: Na_xWO_3

A much studied metal to non-metal transition occurs in the sodium tungsten bronzes as a function of sodium content: for example, Na_xWO_3 undergoes a transition from a non-metallic state to a metallic state as the sodium concentration is increased through $x = 0.25$.^{34,48} These transition metal oxides are non-stoichiometric, with the Na atoms located at interstitial sites in the WO_3 lattice. Consequently, a variety of crystal structures can be obtained depending on the Na concentration. The basic electronic structure is quite similar to that described above for V_2O_3 , namely there is a filled O 2p band well separated from the transition metal d bands.³⁴ In pure WO_3 the gap is approximately 2 eV wide.³⁴ As Na is introduced into the lattice, it ionizes and donates its 3s electron into the W 5d band. This simple band model then predicts that Na_xWO_3 will be metallic. This is indeed the case for high Na concentration. However, for low Na concentrations, non-metallic behaviour is observed.

Numerous explanations have been proposed for both the lack of metallic conductivity at low Na concentrations, and the transition to metallic conduction as the concentration increases. Mott discussed three possibilities: (i) the random location of the Na^+ ions leads to a random charge distribution, resulting in Anderson localization in the conduction band; (ii) an impurity band is formed which is localized for low values of x ; or finally (iii) an impurity band is formed that is split as a result of electron correlations, leading to a gap.⁴⁹ Since each of these cases requires a specific electronic structure, it is clear that photoemission spectroscopy should be able to make a significant contribution to resolving the origin of the composition-induced transition in Na_xWO_3 .⁵⁰

Hollinger *et al.* have performed an extensive photoemission study of the transition in Na_xWO_3 , and of the related transition in the Ta substituted tungsten bronze $\text{Na}_x\text{Ta}_y\text{W}_{1-y}\text{O}_3$.⁵⁰ The advantage of studying the latter system is that there is no change in lattice symmetry (cubic) through the metal to non-metal transition.⁵¹ Since Ta has one less d-electron than W, the d-band is populated by $x - y$ electrons in $\text{Na}_x\text{Ta}_y\text{W}_{1-y}\text{O}_3$. AIP spectra in this study were recorded with a 2D display type analyser with a resolution of 250 meV for valence band spectra, and the emission was excited with synchrotron radiation. The Na_xWO_3 and $\text{Na}_x\text{Ta}_y\text{W}_{1-y}\text{O}_3$ crystals used in the study were cleaved in UHV to expose the (100) plane. If defects appear at the surface of these oxides, they lead to emission in the bulk band gap between the W 5d and the O 2d bands.⁵²

Fig. 12 shows a series of AIP spectra from Na_xWO_3 as a function of Na concentration x .⁵⁰ The photon energy was 60 eV. Fig. 13 shows a similar set of spectra for $\text{Na}_x\text{Ta}_y\text{W}_{1-y}\text{O}_3$. Each figure shows the raw spectra in panel (b), aligned as usual at E_F , while panels (a) in both figures show the spectra with the background subtracted, and shifted in energy to align the high energy sides of the spectra. Examination of the spectra in Fig. 12 and Fig. 13 reveal that when the materials are in the non-metallic (semiconducting) state, the width of the valence band remains constant at 1.1 eV, despite the variation in x or $x - y$. Furthermore, it is clear that the shape of the d-band emission when in the non-metallic state is much more symmetric than when the materials are in the metallic state. The gap between the O 2p and W 5d states is estimated from the photoemission spectra to be approximately 1.8 (± 0.15) eV for Na_xWO_3 , and 1.7 (± 0.15) eV for $\text{Na}_x\text{Ta}_y\text{W}_{1-y}\text{O}_3$.

The behaviour of the conduction band emission close to E_F in Fig. 12 and 13 as the

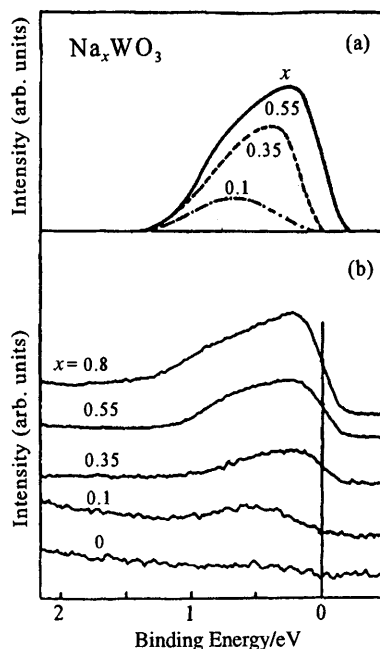


Fig. 12 Series of AIP spectra from Na_xWO_3 as a function of Na concentration, x . $h\nu = 60$ eV. Raw spectra are presented in (b), while (a) presents the spectra following subtraction of the inelastic background.

(Reproduced with permission from *Phys. Rev. B*, 1985, **32**, 1987.)

concentration x or $x - y$ is increased in the semiconducting state cannot be explained by a simple filling of the unoccupied W 5d states.⁵⁰ Rather, the data indicate the development of an impurity band in the W 5d–O 2p band gap as the Na atom concentration increases. For monoclinic WO_3 , the W 5d–O 2p band gap is found to be approximately 2.8 eV, which implies that the Fermi level is pinned just below the bottom of the W 5d conduction band. Fig. 14 shows a schematic density of states for these bronzes in three concentration ranges: (a) semiconducting, with a low Na concentration; (b) semiconducting, with a higher Na concentration, near the metal to non-metal transition; and (c) metallic, for high Na concentrations. States below E_F are occupied, and the shading in the figure indicates Anderson localized states (see Verwey Transition).

The lack of significant lineshape or binding energy changes in the spectra indicate that the states near E_F are almost fully occupied for low x or $x - y$ values. In general, E_F is expected to lie in the middle of an impurity band. The observation of a filled band then implies a splitting of the impurity band into a pair of bands, one of which is filled. This splitting may be the result of correlation effects, with the impurity band split into two Hubbard bands.^{6,7} The lower band is filled, but lies below E_F . This is the situation illustrated in Fig. 14(a). As x or $x - y$ increases, the occupied impurity band begins to overlap the Fermi level. This behaviour is observed experimentally in Fig. 12 and 13 as

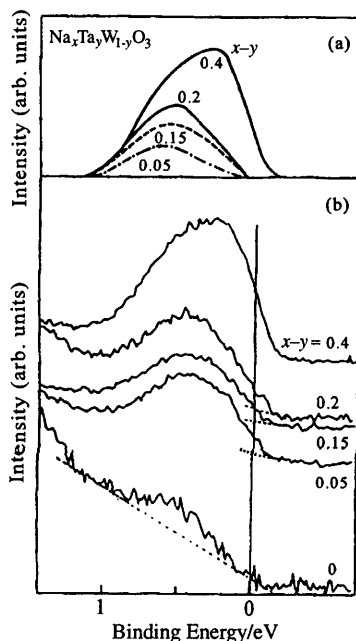


Fig. 13 Series of AIP spectra from $\text{Na}_x\text{Ta}_y\text{W}_{1-y}\text{O}_3$ as a function of Na concentration, x , and Ta concentration, y . $h\nu = 60$ eV. Raw spectra are presented in (b), while (a) presents the spectra following background subtraction.

(Reproduced with permission from *Phys. Rev. B*, 1985, 32, 1987.)

the Na concentration increases, but the materials remain semiconducting. However, such samples ($x - y = 0.20$ and 0.15) still have a thermally activated conductivity. This can be explained by a localization of the states close to E_F . The localization is of the Anderson type, and is a result of the random distribution of Na^+ (and Ta^{5+}) ions. This intermediate situation is illustrated in Figure 14(b). Finally, when the Na concentration is large, the impurity band merges into the W 5d conduction band, although the states near the bottom of the band may remain localized [Fig. 14(c)].

Thus by using photoemission spectroscopy, the nature of the metal to non-metal transition in the sodium tungsten bronzes can be identified as being related to an Anderson transition in the presence of electron correlation: namely in the semiconducting state the gap is between the lower Hubbard and the conduction band, rather than between two Hubbard bands.⁵⁰

Peierls Transitions in Quasi-1D Solids: $\text{K}_{0.3}\text{MoO}_3$ and $(\text{DCNQI})_2\text{Cu}$

The next examples involve quasi-1D solids, which are 3D solids that exhibit 1D characteristics, particularly in their electronic transport properties. Two representative systems will be discussed: the transition metal oxide bronze $\text{K}_{0.3}\text{MoO}_3$, and the organic conductor $\text{DMe}-(\text{DCNQI})_2\text{Cu}$, where DMe-DCNQI denotes dimethyl-

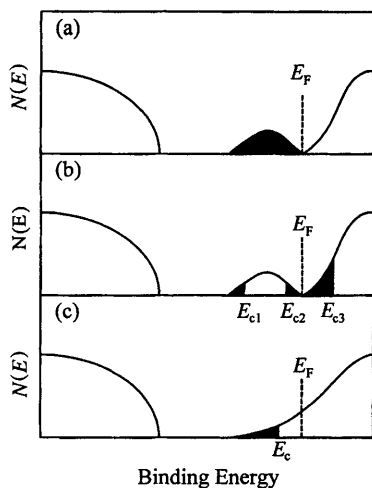


Fig. 14 Schematic band diagram for the sodium tungsten bronzes. (a) and (b) are semiconducting, while (c) is metallic. Anderson localized states are shaded. See text for details.

(Reproduced with permission from *Phys. Rev. B*, 1985, **32**, 1987.)

dicyanoquinonediimine. Each displays Peierls transitions that have been studied using photoemission spectroscopy.

$\text{K}_{0.3}\text{MoO}_3$

In sharp contrast to the sodium tungsten bronzes just discussed (Na_xWO_3 and $\text{Na}_x\text{Ta}_y\text{W}_{1-y}\text{O}_3$) which are 3D conductors in their metallic state, the potassium molybdenum bronze $\text{K}_{0.3}\text{MoO}_3$ is a quasi-1D conductor.^{12–14} $\text{K}_{0.3}\text{MoO}_3$ is one of a family of molybdenum oxide bronzes which display either quasi-1D or quasi-2D electronic properties.^{12–14} While the sodium tungsten bronzes exhibit a metal to non-metal (Anderson-like) transition as a function of Na composition, the quasi-1D molybdenum bronzes exhibit a metal to non-metal transition as a function of temperature that is believed to be a Peierls transition. The basic electronic structure of $\text{K}_{0.3}\text{MoO}_3$ is a matter of some controversy at present, and the results of two sets of photoemission experiments investigating this electronic structure and the properties of the Peierls transition will be discussed here. For a review of ARP applied to quasi-low dimensional conductors, see ref. 53.

The quasi-low dimensional properties of the molybdenum oxide bronzes are related to their complex crystal structure: they are layered materials, with slabs of MoO_6 octahedra separated by sheets of A cations (A = monovalent metals).^{12–14,54} The Mo bronzes can be divided into three broad classes based upon their composition and common properties: blue bronzes, purple bronzes and red bronzes. The blue bronzes have a common structure $\text{A}_{0.3}\text{MoO}_3$ with A = K, Rb or Tl, the purple bronze structure is $\text{A}_{0.9}\text{Mo}_6\text{O}_{17}$ with A = Li, Na, K and Tl, and the red bronze structure is $\text{A}_{0.33}\text{MoO}_3$ with A = Li, K, Cs, Rb and Tl. In the blue bronzes the MoO_6 octahedra are primarily

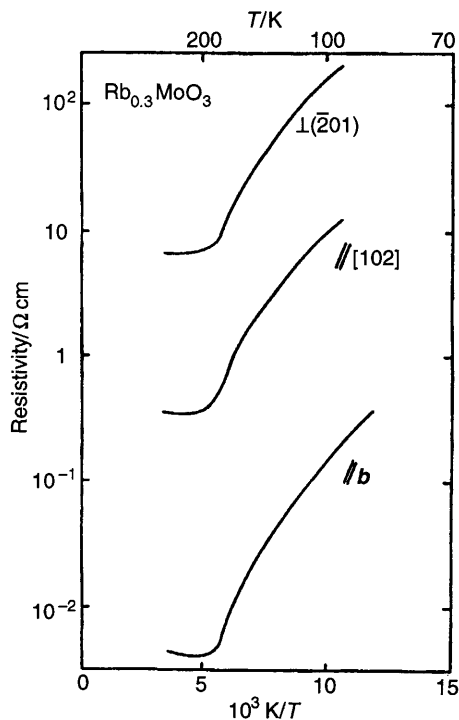


Fig. 15 Resistivity as a function of temperature for $\text{Rb}_{0.3}\text{MoO}_3$ along various crystallographic axes.

(Reproduced with permission from *Crystal Chemistry and Properties of Materials with Quasi-one-dimensional Structures*, Reidel, Dordrecht, 1986 and *J. Phys. Lett.*, 1973, **44**, L113.)

bonded through corner sites along the crystallographic b axis and these bronzes display quasi-1D properties.⁵⁴ By contrast, in the purple bronzes, the MoO_6 octahedra form corner bonded two dimensional networks, and quasi-2D effects are observed.⁵⁴

Fig. 15 shows the temperature variation of the resistivity of $\text{Rb}_{0.3}\text{MoO}_3$ for current flowing along three mutually perpendicular axes in the crystal; the transport properties of $\text{K}_{0.3}\text{MoO}_3$ are essentially identical.^{13,55,56} As is clear, the resistivity just below room temperature is two orders of magnitude higher for current flowing perpendicular to the planes as opposed to within the planes. Also clearly visible in Fig. 15 is a metal to non-metal transition that has an onset on cooling at approximately 180 K. X-Ray scattering studies of the crystal structure of $\text{K}_{0.3}\text{MoO}_3$ reveal the existence at 180 K of well defined superlattice peaks, indicating a structural instability of the lattice with temperature, and is used to support the identification of the metal-insulator transition as a Peierls transition.^{55,56}

There have been numerous photoemission studies of $\text{K}_{0.3}\text{MoO}_3$ and some aspects of the electronic structure of this material are now well understood.⁵⁷⁻⁶³ In particular, the structure of defects in $\text{K}_{0.3}\text{MoO}_3$ has been extensively investigated recently, and is

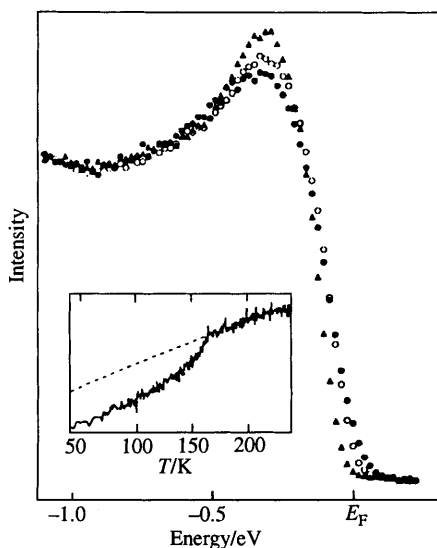


Fig. 16 Photoemission spectra from $K_{0.3}MoO_3$ for various temperatures: (\blacktriangle) 80 K, (\circ) 183 K, (\bullet) 313 K. Inset shows temperature dependence of the spectral intensity at 70 meV below E_F .

(Reproduced with permission from *Europhys. Lett.*, 1992, **19**, 525.)

discussed in Section 5 in the context of a novel defect induced metal to non-metal transition at the surface.^{62,63} $K_{0.3}MoO_3$ cleaves easily and exposes a $(20\bar{1})$ plane, and the surface is highly sensitive to electron, ion, and photon beam damage. The Peierls transition in $K_{0.3}MoO_3$ has been studied using partially angle integrated photoemission by Dardel *et al.*^{57,58} Fig. 16 shows a series of photoemission spectra from cleaved $K_{0.3}MoO_3$ for temperatures above and below the Peierls transition temperature. The samples used in these experiments were cleaved in UHV, and the photoemission spectra taken using a 200 mm SDA-type analyser. The angular acceptance of the analyser used was ± 3 degrees. In this regime both density of states and band effects may occur simultaneously in the spectra. The analyser had an overall energy resolution of approximately 20 meV. The spectra were taken with an He I discharge lamp, with $h\nu = 21.2$ eV. Emission between approximately 1 eV and E_F originates from the Mo 4d states that form the Fermi surface. The O 2p band lies between 2.5 and 8 eV below E_F . There is a bulk band gap between the Mo 4d and O 2p states.

It is clear that for the spectra in Fig. 16, there is virtually no emission at E_F , despite the room temperature metallic nature of $K_{0.3}MoO_3$. Thus, unlike V_2O_3 , the observation of the gap formation is difficult, since the spectra seem to indicate the existence of a gap at room temperature. However, it is also clear from Fig. 16 that as the crystal is cooled through $T_c = 180$ K, the spectra do change somewhat. Spectral weight can be seen to be transferred from close to E_F to higher binding energy as the sample is cooled below

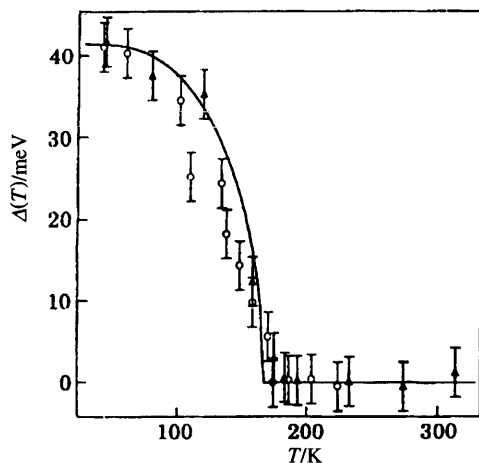


Fig. 17 Temperature dependence of the parameter $\Delta(T)$ for $\text{K}_{0.3}\text{MoO}_3$ (\blacktriangle) and $\text{Rb}_{0.3}\text{MoO}_3$ (\circ). The solid line is the normalized BCS gap; $T_c = 167$ K. (Reproduced with permission from *Europhys. Lett.*, 1992, **19**, 525.)

T_c . Significantly, the spectra show changes down to 0.5 eV below E_F . This energy scale is much larger than that anticipated for the opening of the Peierls gap, approximately 50–75 meV. The inset in Fig. 16 shows the temperature variation of the intensity of the spectra at a fixed binding energy of 70 meV. There is a clear discontinuity at a temperature that correlates well with the onset of the bulk Peierls transition as observed in resistivity measurements (in air).⁵⁸

Study of the development of the Peierls gap is complicated by the intrinsic width of the Mo 4d photoemission feature. To circumvent this, Dardel *et al.* consider the behaviour of the inflection point of the emission close to E_F , and define a phenomenological parameter $\Delta(T)$ which is the shift of this inflection point away from its position at $T = 183$ K. Fig. 17 shows the temperature dependence of $\Delta(T)$. Above T_c , $\Delta(T)$ shows no significant variation with temperature, while it varies rapidly below T_c , corresponding to the changes in spectra. While this is a purely phenomenological parameter, it shows a temperature variation very similar to that of a BCS gap, which is plotted in Fig. 17 as a solid line.

Although the focus in this review is on the Peierls transition in $\text{K}_{0.3}\text{MoO}_3$, it is worth pointing out that the low emission intensity at E_F displayed by the spectra in Fig. 16 for $\text{K}_{0.3}\text{MoO}_3$ in the metallic state has prompted significant debate centring on whether this lack of emission is related to the electronic ground state of a 1D metal, or whether it has its origin in other physical aspects of the material itself. The expectation that there should be a Fermi edge visible in photoemission spectra from these metals is based on an assumption that the quasi-particle band picture described in Section 3 applies in 1D. However, the correct model for an exactly 1D metal is that of the Luttinger liquid.⁶⁴ The salient feature of this theory is that in 1D the electron spin and charge are decoupled, and the spectral function has vanishing weight at E_F . For a non-correlated Fermi liquid, the spectral function for a quasi-particle at E_F is simply a delta function.

As correlations increase, the delta function is lost, and some weight is transferred to excitations away from E_F . However, in the Luttinger picture, all the weight is transferred away from E_F into collective excitations of the system.⁶⁴ Thus for a true 1D metal, there is no Fermi edge in the electron density of states, and much of the recent interest in these photoemission studies has been motivated by the belief that the Luttinger liquid state was being observed.^{57,58} $K_{0.3}MoO_3$ is very sensitive to surface defects. These defects (either O vacancies, or variations in K content on the cleaved surface) strongly modify the photoemission intensity at E_F .^{62,63} This is because in these layered, large unit cell materials, photoemission spectroscopy primarily measures the electronic structure of the topmost layer only. Thus, while the work of Dardel *et al.* aims at measuring the bulk Peierls transition, it is in fact the electronic structure of only the outer layer that is being probed. (This is a complication not suffered by the 3D systems discussed elsewhere in this article, since the bulk wavefunctions will extend to the crystal surface.) The low emission intensity at E_F can thus have an origin other than the Luttinger liquid ground state, such as non-stoichiometric surfaces.

DMe-(DCNQI)₂Cu

Many organic solids display resistivity transitions (including superconducting transitions), but their study with photoemission spectroscopy is often difficult due to the poor quality of the crystal surfaces. Nevertheless, photoemission has been successfully applied in a number of cases. One such class of solids is the (DCNQI)₂Cu salts, which are quasi-1D solids consisting of chains of $p\pi$ DCNQI (dicyanoquinonediimine) linked by Cu 3d orbitals.⁶⁵ Deuteriated dimethyl (DMe-) salts exhibit a sharp metal to non-metal transition at 80 K.⁶⁶ The transition is accompanied by a PLD, which is associated with ordering of Cu^+ and Cu^{2+} states; these salts are of mixed valency with an average $Cu^{(4/3)+}$ ion in both the metallic and non-metallic states.

Fig. 18 shows the valence band photoemission spectrum from room temperature DMe-(DCNQI-d)₂Cu. The analyser was an SDA, and an He I resonance lamp giving $h\nu = 21.2$ eV was used as the radiation source. Samples were single crystals fractured in UHV, but they did not cleave well. Consequently, the authors assert that their spectra are representative of the density of states, since the angular emission from the rough surface will be random, thus integrating over k -space. The dominant peak at 8 eV originates from the C and N 2p σ states, while the emission at 4 eV originates from the Cu 3d states. Fig. 19 shows the temperature dependence of the emission close to E_F as the sample is cooled through the metal to non-metal transition at 80 K. The spectrum for the sample at 55 K indicates the possible existence of a gap of approximately 100 meV in the non-metallic phase.⁶⁵

While there are clear variations in the emission intensity near E_F through the transition, the emission is almost zero at E_F , even in the metallic phase. Again, this is cited as possibly being due to Luttinger liquid effects.⁶⁴ The data are analysed in the context of this model in the original publication. However, as with $K_{0.3}MoO_3$, the possibility that the poor quality of the surface under investigation is the origin of the lack of emission at E_F is not considered and deserves further study.⁵³

Partial Peierls Transitions in Quasi-2D Solids: 1T-TaS₂ and Na_{0.9}Mo₆O₁₇

As mentioned earlier, a noteworthy difference between quasi-1D and quasi-2D systems is that while metal to non-metal transitions occur in quasi-1D solids, many quasi-2D

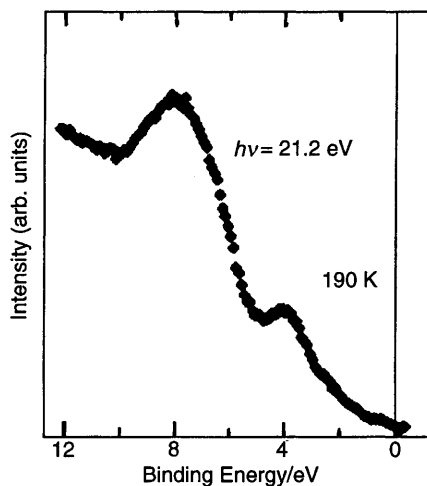


Fig. 18 Valence band spectrum from DMe-(DCNQI-d₇)₂Cu. (Reproduced with permission from *Phys. Rev. B*, 1995, **51**, 13 899).

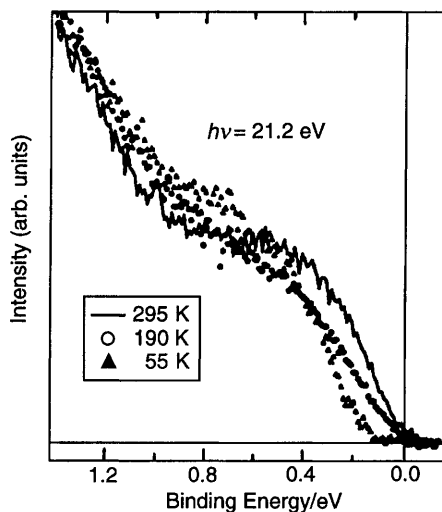


Fig. 19 Series of photoemission spectra from DMe-(DCNQI-d₇)₂Cu for various temperatures. See text for details. (Reproduced with permission from *Phys. Rev. B*, 1995, **51**, 13 899).

systems exhibit metal to metal transitions due to the opening up of a gap over only part of the Brillouin zone. In this section, the application of photoemission spectroscopy to two quasi-2D systems will be described. In the first of these, 1T-TaS₂, the evolution of

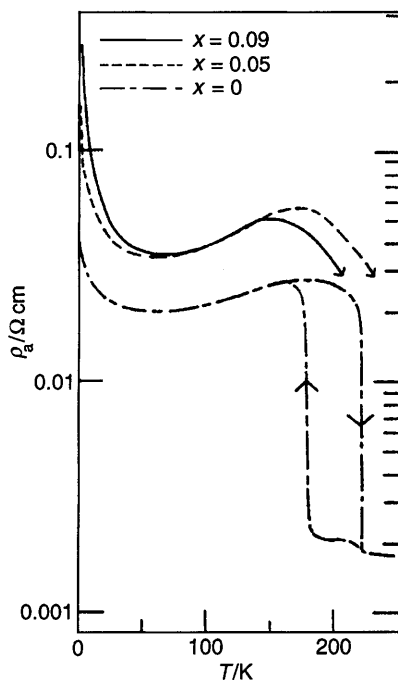


Fig. 20 Resistivity (ρ_a) as a function of temperature for pure and Se-doped 1T-TaS₂. (Reproduced with permission from *Physica B*, 1980, **99**, 173.)

the band structure close to E_F has been studied during the resistivity transition, while in the second, Na_{0.9}Mo₆O₁₇, photoemission has been used to measure the full Fermi surface driving the metal to metal transition.

1T-TaS₂

Fig. 20 shows the resistivity *versus* temperature behaviour of 1T-TaS₂.⁶⁷ This material undergoes a particularly complex series of lattice distortions with changes in temperature, determined by the structure of the quasi-2D Fermi surface. For temperatures below 550 K, 1T-TaS₂ is in a PLD state. For temperatures between 350 and 550 K, the associated CDW is incommensurate with the lattice, while it has a quasi-commensurate structure between 180 and 350 K. Below 180 K, 1T-TaS₂ has a $\sqrt{13} \times \sqrt{13}$ commensurate structure.^{68,69} Associated with the 180 K CDW transition is a metal to metal transition exhibiting a ten-fold increase in resistivity, while at 60 K the resistivity shows a large increase in a metal to non-metal transition.

That the large changes in the band structure and Fermi surfaces required for the metal to metal transition occur at the quasi-commensurate to commensurate CDW transition indicates that mechanisms other than a simple Peierls transition are involved. Electron correlations within the CDW bands and disorder at low tempera-

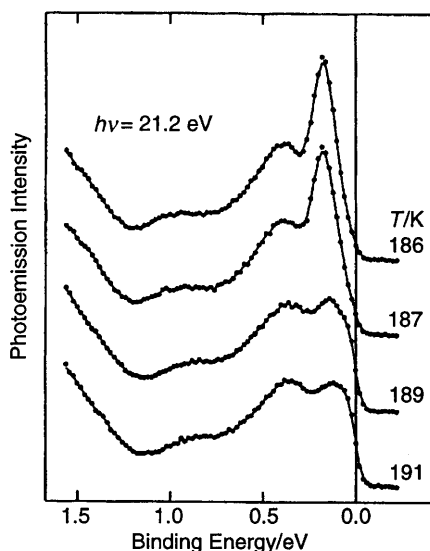


Fig. 21 Photoemission spectra for 1T-TaS₂ at the quasi-commensurate to commensurate CDW transition on cooling.
(Reproduced with permission from *Phys. Rev. B*, 1997, **45**, 1462.)

tures are believed to play a significant role in 1T-TaS₂, and a Mott localization is believed to occur at the quasi-commensurate to commensurate CDW transition. Much of the evidence for this comes from photoemission spectroscopy.^{70,71}

Fig. 21 presents a series of photoemission spectra from 1T-TaS₂ taken for temperatures around the quasi-commensurate to commensurate CDW transition by Dardel *et al.*⁷⁰ The sample was cleaved in UHV, the energy resolution of the SDA spectrometer was 15 meV for a sample at 20 K, and the angular resolution was ± 3 degrees. The spectra are thus only partially angle integrated, but can be related to the density of states with caution. The spectrum from the quasi-commensurate phase at 191 K clearly shows emission at E_F , while this emission intensity is greatly reduced in the spectrum taken at 186 K. (The structure in the photoemission spectrum for the quasi-commensurate phase have been shown to be the result of the CDW modulation of the band structure.⁷²) The dramatic changes in the spectra with only a 5 K change in temperature clearly indicate a radical change in electronic structure associated with the quasi-commensurate to commensurate CDW transition.

At first sight the development of the sharp peak at 180 meV below E_F in the low temperature phase seems to agree with a model for this transition that involves a Mott localization of the electrons due to correlation within the CDW state. The peak is interpreted as emission from the lower Hubbard band, which would indicate a gap of approximately 150–200 meV in the commensurate phase. However, a gap of this size is inconsistent with the resistivity data in the commensurate phase (Fig. 20). Closer examination of the intensity at E_F indicates that while it is small in the commensurate phase, it is not zero. Fig. 22 shows the temperature dependence of the emission intensity

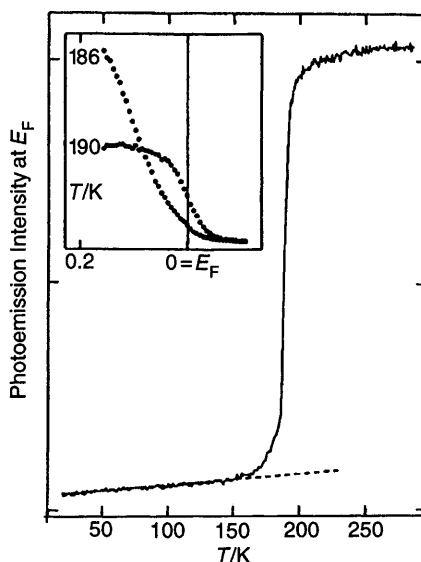


Fig. 22 Temperature dependence of the photoemission intensity at E_F for 1T-TaS₂. The inset shows the spectra for sample temperatures above and below the quasi-commensurate to commensurate CDW transition. (Reproduced with permission from *Phys. Rev. B*, 1992, **45**, 1462.)

at E_F , and representative spectra within 200 meV of E_F .⁷⁰ The finite emission in the commensurate phase indicates that the Mott transition does not completely open a gap. Rather, there is a pseudogap in the structure, and the density of states in the gap varies with temperature. Thus the transport properties at low temperatures are governed not by the Mott localized electrons far from E_F , but rather by the residual electrons at E_F .⁷⁰

Note also that the resistivity transitions show a strong hysteresis, and that these are also easily studied using photoemission spectroscopy. Fig. 23 shows the intensity at E_F and at 180 meV below E_F plotted as a function of temperature as the crystal temperature is cycled.⁷¹ The similarities between these curves and the bulk resistivity curves (shown as an inset) are striking. The small step structures visible in the photoemission hysteresis curves are interpreted as due to surface phenomena, requiring further study.⁷¹

$\text{Na}_{0.9}\text{Mo}_6\text{O}_{17}$

$\text{Na}_{0.9}\text{Mo}_6\text{O}_{17}$ is a quasi-2D transition metal oxide bronze that exhibits a metal to metal transition at 80 K, accompanied by a PLD. The resistivity data are presented in Fig. 24. $\text{Na}_{0.9}\text{Mo}_6\text{O}_{17}$ possesses a layered structure consisting of planes of Mo–O polyhedra separated by Na ions.⁵⁴ The Mo 4d states are occupied by electrons donated from the Na ions. The transition and the PLD are believed to be a consequence of so-called hidden Fermi surface nesting, as was described earlier.¹⁸ In this section we discuss a direct measurement of this hidden Fermi surface nesting.⁷³

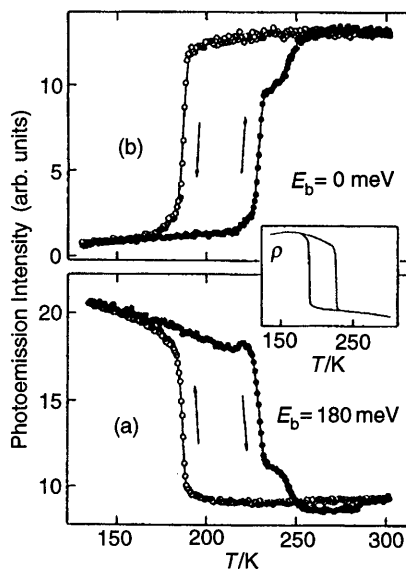


Fig. 23 Variation of the photoemission spectral intensity at E_F and at 180 meV below E_F , as a function of temperature on both cooling (\circ) and heating (\bullet). Inset shows $\rho(T)$. (Reproduced with permission from *Phys. Rev. B*, 1992, **45**, 7407.)

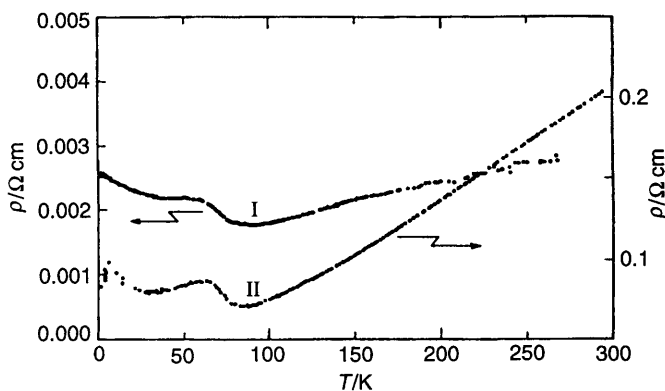


Fig. 24 Temperature variation of the resistivity (ρ) of $\text{Na}_{0.9}\text{Mo}_6\text{O}_{17}$. (I) ρ parallel to MoO_6 cleavage planes; (II) ρ perpendicular to MoO_6 planes. (Reproduced with permission from *Chem. Rev.*, 1988, **88**, 31.)

The Fermi surface was measured using ARP, and the experiments were performed on crystals cleaved in UHV. Fermi surface mapping was performed in the conventional manner by defining a point on the Fermi surface by the location in k -space where emission from a particular band disappears as the associated band disperses above E_F .

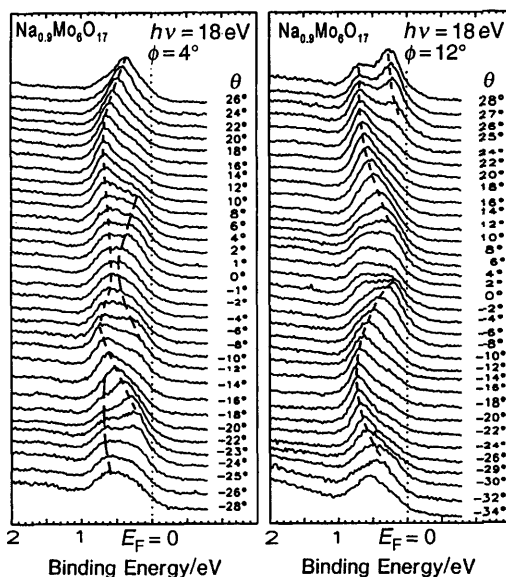


Fig. 25 ARP spectra from cleaved $\text{Na}_{0.9}\text{Mo}_6\text{O}_{17}$. $h\nu = 18\text{ eV}$, incident at 45° to the sample normal in the $\Gamma Y'$ plane. Variations in θ and ϕ correspond approximately to the $\Gamma Y'$ and $\Gamma X'$ directions in the Brillouin zone, respectively. See text for details. The surface Brillouin zone is shown in Fig. 26.

(Reproduced with permission from *Phys. Rev. Lett.*, 1996, **76**, 3172.

Fig. 25 shows two representative sets of ARP spectra taken with 18 eV photons. Only the energy region close to E_F is shown, and the spectral feature is due to emission from Mo 4d states. The onset of the O 2p emission occurs at 2.5 eV. Variation of the spectrometer angle θ corresponds to detecting electrons with momenta approximately along the $\Gamma Y'$ direction in the projected bulk Brillouin zone, while variation of the spectrometer angle ϕ corresponds to detecting electrons with momenta approximately along the $\Gamma X'$ direction. (The Brillouin zone and symmetry labels are shown in Fig. 26.) All angles are measured relative to the sample normal. Fig. 25 presents data for two different values of ϕ , with θ varied in 2 degree steps, and corresponds to scanning through the Brillouin zone in two slices, parallel to $\Gamma Y'$. The full data set consists of many hundreds of spectra, with scans taken both parallel and perpendicular to $\Gamma Y'$.

The spectra in Fig. 25 show particularly clear band dispersion for a transition metal oxide. There are three occupied Mo 4d bands in $\text{Na}_{0.9}\text{Mo}_6\text{O}_{17}$, which are predicted to form three distinct Fermi surface structures as they cross E_F .⁷⁴ Consequently, the Mo 4d spectral feature comprises emission from up to three bands, depending on the location in the Brillouin zone. As a guide to the eye, the dispersion of the primary features of the spectra have been marked. Considering the $\phi = 12$ degree set of spectra in Fig. 25, a symmetric dispersive feature is clearly visible on both sides of $\theta = 0$ degrees. This is designated as band 1. As θ is varied from -30 to -20 degrees, band 1 disperses away from E_F to higher binding energies, reaching a maximum binding energy of

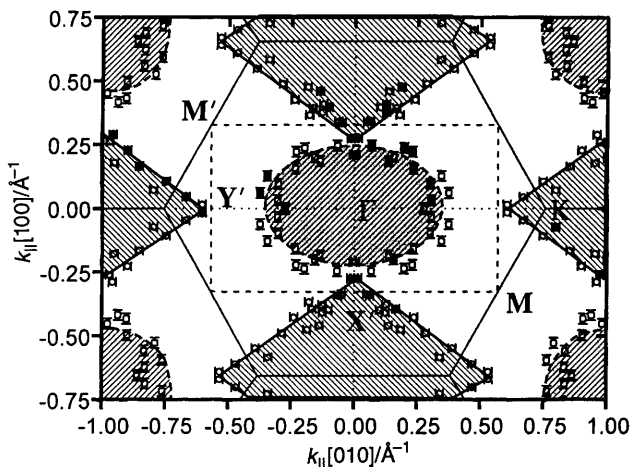


Fig. 26 Measured Fermi surface of $\text{Na}_{0.9}\text{MoO}_{1.7}$. Band 1 data (●), band 2 data (■); hollow symbols indicate symmetry mapped points. The projected monoclinic and pseudo-hexagonal Brillouin zones are indicated. See text for details. (Reproduced with permission from *Phys. Rev. Lett.*, 1996, **761**, 3172.)

700 meV, then disperses back towards E_F as θ approaches zero, disappearing above E_F at approximately -4 degrees. The peak reappears for $\theta > +4$ degrees, and proceeds to disperse to higher binding energies. Clearly band 1 forms a hole pocket in the Fermi surface centred around the $\Gamma X'$ axis ($\theta = 0$ degrees). (Note that the Γ point is $\theta = 0$, $\phi = 0$ degrees.) The spectra in the left hand panel of Fig. 25 are equivalent to the spectra in the right hand panel, but with $\phi = 4$ degrees. Thus these spectra also show emission from states in a slice through the zone parallel to $\Gamma Y'$, but closer to Γ . Here, band 1 approaches, but does not cross E_F , indicating the closure of the hole pocket.

By scanning the entire surface Brillouin zone in a manner similar to that described above, the full Fermi surface was measured, and is presented in Fig. 26. Here crossings of E_F by band 1 are displayed as circles, while crossings of a second band observed in spectra not shown here, are indicated as squares. Filled symbols correspond to the measured data points, hollow symbols indicate symmetry mapped points. (The choice of unit cell and the validity of these symmetry operations are discussed in the original report.⁷³) The measured Fermi surface consists of two distinct types of structures: a closed electron pocket (roughly elliptical in shape) around Γ , and hole pockets (roughly diamond shaped) along $\Gamma X'$ and $\Gamma Y'$. (Note that the lines drawn in Fig. 26 are guides to the eye, and not fits to the data points; they emphasize the observation of two distinct types of structure.)

Inspection of Fig. 26 shows that the Fermi surfaces of the electron and hole pockets can be combined to form almost uninterrupted pseudo-1D Fermi surfaces parallel to the $\Gamma M'$ axes of the rectangular zone. These 1D Fermi surfaces are drawn in Fig. 27, where the same data points are shown as in Fig. 26. A pair of lines running parallel to $\Gamma M'$ connects both the electron and hole structures shown in Fig. 26. This is precisely the hidden Fermi surface nesting predicted by Whangbo *et al.*¹⁸ The nesting of this

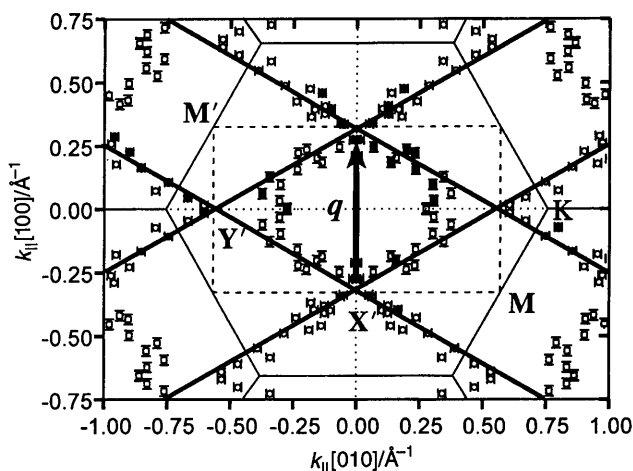


Fig. 27 Same data as Fig. 26, with pseudo-1D Fermi surface structures drawn. The vector q nests both pairs of Fermi surface.
(Reproduced with permission from *Phys. Rev. Lett.*, 1996, **76**, 3172.)

hidden Fermi surface corresponds to the displacement vectors that are associated with the superlattice spots observed below the critical temperature for the Peierls transition. As can be seen in Fig. 27, two pairs of quasi-1D Fermi surface segments can be connected to each other by the same vector q , thereby maximizing the nesting. To within experimental error, the measured quasi-1D nesting vector ($2k_F = 0.67 \text{ \AA}^{-1}$) is essentially identical to both the predicted value, and also to the displacement vector given by the $\text{KMnO}_6\text{O}_{17}$ X-ray diffraction data.^{18,75} This measurement verifies the concept of hidden Fermi surface nesting, and thus supports the identification of the metal-metal transitions in inorganic and organic quasi-2D conductors as Peierls transitions. Section 6 considers the future of such measurements.

Verwey Transition in Fe_3O_4

Fe_3O_4 undergoes an abrupt two order of magnitude decrease in resistivity as the temperature is increased through $T_V = 120 \text{ K}$. This behaviour is illustrated in Fig. 3. Photoemission spectroscopy has been used on numerous occasions to measure the room temperature electronic structure of Fe_3O_4 , and recently it has been used to study the nature of the Verwey transition itself. Two such studies will be discussed here.

Fig. 28 shows three photoemission spectra measured by Chainani *et al.* from Fe_3O_4 .⁷⁶ The lower spectrum is taken using He I radiation at 21.2 eV , and with the sample held at 100 K , below T_V . The upper two spectra are taken with the sample held at 140 K , above T_V ; the middle spectrum was acquired with He I radiation at 21.2 eV , while the upper spectrum was taken with He II radiation at 40.8 eV . These spectra are all taken with a 150 mm SDA-type analyser, and can be considered to be partially angle integrated, and therefore partially representative of the density of states. The samples were single crystals, fractured in UHV to expose the (110) surface and the $(\bar{1}10)$ surface

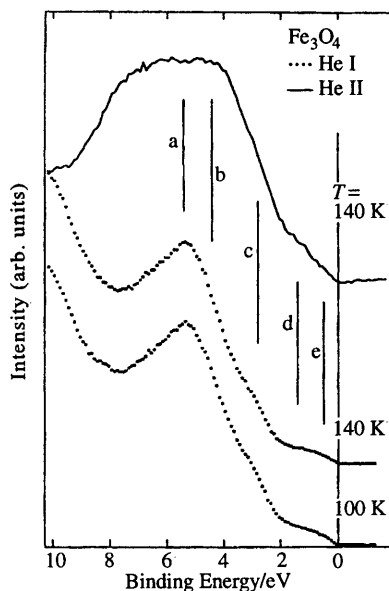


Fig. 28 Photoemission spectra from Fe_3O_4 above and below the Verwey transition taken with 21.2 eV (He I) and 40.8 eV (He II) photons. Feature a is primarily emission from O 2p states, while features b \rightarrow e are due to Fe 3d. (Reproduced with permission from *Phys. Rev. B*, 1995, **51**, 976.)

facets (Fe_3O_4 does not cleave easily). The Fe 3d states and O 2p states are significantly hybridized, and the emission feature between 2 and 8 eV below E_F in the spectra is derived from these states.⁷⁷ The states labelled d and e in Fig. 28 have been identified using spin-polarized photoemission spectroscopy as Fe 3d in character, with d originating from majority spin e_g states, and e from minority spin t_{2g} states.⁷⁸ Fig. 29 shows the spectral changes close to E_F as a function of temperature. Included in the inset of this figure is the spectrum from polycrystalline gold as an indication of the behaviour of normal metal, and as a calibration of E_F .

The 100 K spectrum indicates a gap of approximately 70 meV, roughly half the activation energy. This in turn implies that E_F is pinned half way in the gap. The existence of defects, such as O vacancies, can be assumed on the surface due to the poor cleaving properties.⁷⁹ Typically, O vacancies act as electron traps, and pin E_F just below the conduction band. Consequently, this report of mid-gap pinning is a surprise. Examination of the 140 K spectrum in Fig. 29 reveals emission intensity at E_F . Chainani *et al.* consider this evidence for a finite density of states at E_F at 140 K, and thus evidence for a clear metal to non-metal transition in Fe_3O_4 . As discussed in Section 2, this transition is attributed to a loss of long range order with increasing temperature. The fact that the emission at E_F increases in intensity as the temperature is increased up to room temperature, is used as evidence for persistent short range order above T_v .⁷⁶

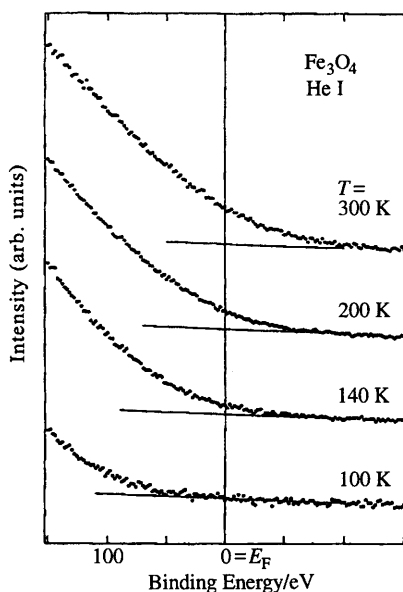


Fig. 29 Series of photoemission spectra from Fe_3O_4 for energies close to E_F as the temperature is varied.
(Reproduced with permission from *Phys. Rev. B*, 1995, **51**, 976.)

However, the results presented in Fig. 28 and 29 are not reproduced in the experiments of Park *et al.*^{37,80} Fig. 30 shows a wide energy scan of the emission from Fe_3O_4 taken with 110 eV photons from a synchrotron light source. The crystal in this experiment was fractured to expose the (100) surface, which is reported to show less faceting than the (110) surface.^{37,80} As with the data of Chainani *et al.*, spectra were taken with a 150 mm SDA-type analyser, although by using higher energy photons (> 100 eV) the spectra can be considered more representative of the density of states. (This point was discussed in Section 3.) Fig. 30 actually shows two spectra, taken on either side of T_v , one with the crystal at 100 K, the other for the crystal at 130 K. The spectra are almost identical. Fig. 31 shows the emission close to E_F for the same temperatures. One significant difference between the data of Chainani *et al.* (Fig. 29) and Park *et al.* (Fig. 31) is that the state close to E_F (labelled μ for the chemical potential by Park *et al.*) is clearly resolved in Fig. 31, but is only a shoulder in Fig. 29. This may reflect the reported higher quality of the surfaces (lower density of defects), or it may be a function of different crystallographic surfaces under investigation. A second difference between these two experiments is the clear observation of a gap at 130 K in the spectra by Park *et al.* The spectrum from polycrystalline copper is shown for comparison with that of a pure metal in Fig. 31, and it is clear that although minor changes in the magnitude of the Fe_3O_4 gap are observed as the temperature is varied through T_v , there is virtually no emission intensity at E_F at 130 K. Park *et al.* also used bremsstrahlung isochromatic spectroscopy (inverse photoemission spectroscopy) to determine the empty density of states, and the position of the bottom of the unoccupied

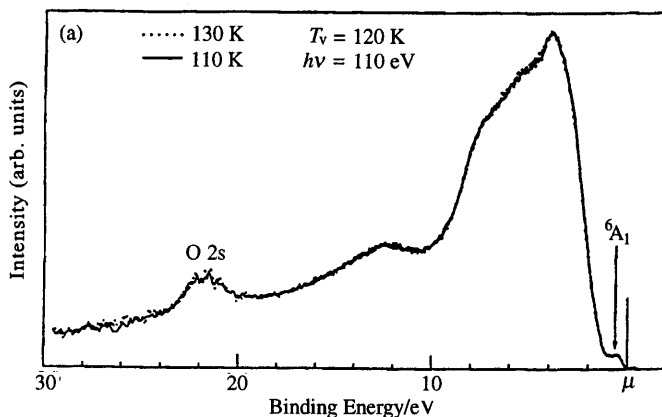


Fig. 30 Photoemission spectra from Fe_3O_4 above and below the Verwey transition, taken with 110 eV photons. See text for details.
(Reproduced with permission from ref. 37.)

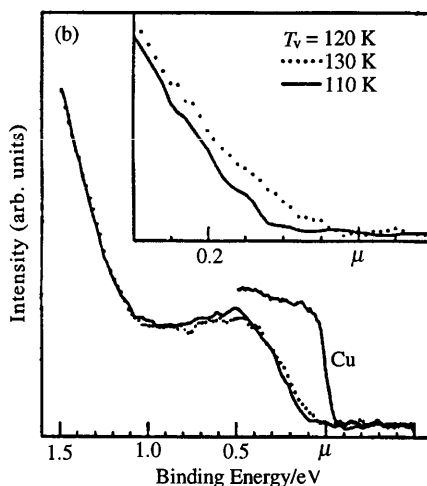


Fig. 31 Photoemission spectra for Fe_3O_4 above and below the Verwey transition for the energy region close to E_F . $h\nu = 110$ eV. Photoemission from clean Cu is shown as an inset. See text for details.
(Reproduced with permission from ref. 37.)

conduction band. They were thus able to make an accurate determination of the gap as being 150 meV at 110 K, and 100 meV at 130 K. This result implies that the Verwey transition is not a metal to non-metal transition, but rather a transition from one semiconducting state to another. Clearly at higher temperatures metallic properties

predominate, but at the actual temperature where the resistivity transition occurs, and the order–disorder transition occurs, a gap persists.

It is difficult to arrive at an experimental artifact that would allow for the persistence of this gap. Given the better quality (100) surfaces, and the fact that higher kinetic energy spectra measured with SDA analysers come closer to measuring the density of states than those of a lower kinetic energy (Section 3), it is probable that the data of Park *et al.* are a more accurate determination of the gap behaviour. However, the example of Fe_3O_4 shows a situation where photoemission spectroscopy has yet to provide definitive and comprehensive information on the origin and nature of a metal to non-metal transition.

5 Metal to Non-metal Transitions at Surfaces

Studies of metal to non-metal transitions at surfaces form a relatively new area of research. As shall be discussed there are a wide variety of such transitions. Three broad classes can be distinguished: (i) the transition from an insulating to a metallic state for adsorbed metal atoms on a surface as the density of the atoms increases; (ii) the transition of a metallic surface layer into an insulating layer by the introduction of defects; and (iii) the modification of bulk metal to non-metal transitions at surfaces by the presence of foreign adsorbates at the surface. Making resistivity measurements of surface layers is not trivial, but since photoemission spectroscopy is inherently surface sensitive, it is an ideal probe of these transitions.

Metal Adsorbate Transitions: Mg on Mo(112)

In principle the adsorption of metal atoms on surfaces provides a model environment to study low dimensional metal to non-metal transitions. At the most fundamental level it is clear that isolated metal atoms on a surface will not form a metallic overlayer, but that at some concentration of adsorbed atoms a conducting overlayer must form. Depending on bonding interactions with the substrate, the geometry of the substrate surface, and the type of metal adsorbed, numerous classes of metal to non-metal transition are possible, including Wilson transitions, Mott transitions, or Peierls transitions.

The study of metal to non-metal transitions on surfaces using a variety of surface sensitive spectroscopies has recently been well reviewed in a series of articles.^{15,81,82} By way of an example of the applicability of photoemission spectroscopy in the study of these transitions, the adsorption of Mg on the Mo(112) surface is considered here.^{83–85} This is an interesting system, since it represents a class of metal to non-metal transitions that occur for metal adsorbates on metal surfaces. Photoemission is used to study the detailed changes in the Mg band structure as the overlayer becomes fully metallic.

Fig. 32 shows a series of ARP spectra from Mg/Mo(112).⁸³ The spectra are taken with an SDA-type analyser with a resolution of approximately 150 meV. Two sets of spectra are presented, for 0.5 and 2.0 monolayers (ML) of Mg. Within each set of spectra, the angle of the detector is varied to probe states at different positions in the surface Brillouin zone, as shown. Mg undergoes a gradual transition to a metallic overlayer as a function of concentration on the Mo(112) surface.^{84,85} The onset of metallic properties occurs at approximately 0.5 ML. Considering the 0.5 ML spectra in

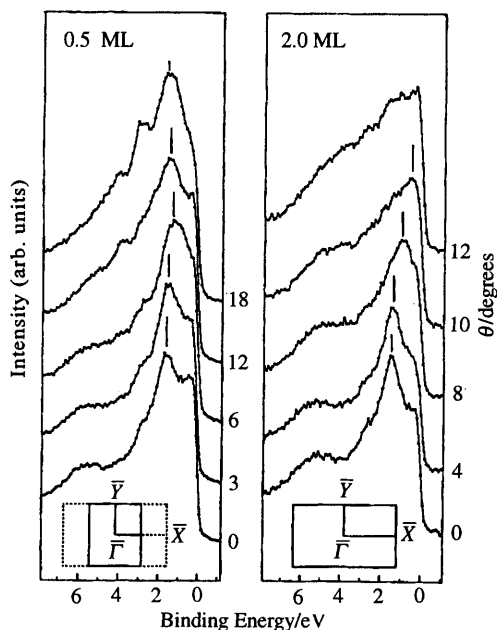


Fig. 32 Series ARP spectra from 0.5 and 2.0 ML Mg films on Mo(112). $h\nu = 70$ eV. The detector was rotated to measure states along the $\bar{\Gamma}$ – \bar{X} direction in the surface Brillouin zone.

(Reproduced with permission from *Europhys. Lett.*, 1995, **29**, 469.)

Fig. 32, the two emission features close to E_F are both Mg-induced surface states, i.e., 2D states, localized at the surface. A normal emission (zone centre), one of these states (denoted 1) is at 1.6 eV, while the other (denoted 2) is at 0.5 eV with respect to E_F . The dispersion of the higher binding energy state is indicated by the vertical line in Fig. 32. The spectra probe states out to the surface Brillouin zone boundary, and it is clear that this state remains far from E_F across the entire zone for the 0.5 ML system. However, examination of the spectra in the right hand panel show that for 2.0 ML of Mg, this state disperses above E_F , thus forming a Fermi surface.

Fig. 33 shows the dispersion of surface state as a function of Mg coverage. The crossing of the Fermi level and the creation of a hole pocket around the \bar{X} point is clearly visible for the 2.0 ML film. Note, however, that the dispersion is much less pronounced along the perpendicular direction in the zone. This is consistent with the geometric structure of the overlayer as probed by low energy electron diffraction, which indicates that the Mg atoms are closer together along the real space direction corresponding to the $\bar{\Gamma}$ – \bar{X} direction in the surface Brillouin zone. The ability to measure clear dispersion of the bands allows an electron effective mass to be extracted from the data. The in-plane effective mass of the electron along the $\bar{\Gamma}$ – \bar{X} direction is $m^*/m_e = 15.7$ for the 0.5 ML film, while it decreases dramatically to $m^*/m_e = 1.68$ for the 2.0 ML film. This quantitative measurement of the changes in the effective mass as a

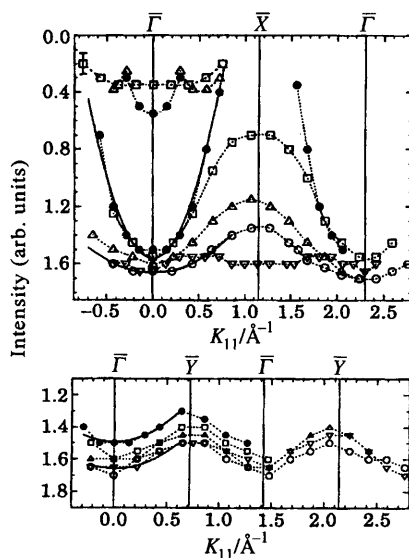


Fig. 33 The measured dispersion of the Mg-induced bands for Mg films on Mo(112) along both the $\bar{\Gamma}$ - \bar{X} (top panel) and $\bar{\Gamma}$ - \bar{Y} (bottom panel) directions in the surface Brillouin zone. (∇) 0.4 ML, (\circ) 0.6 ML, (\triangle) 0.7 ML, (\square) 1 ML and (\bullet) 2 ML. (Reproduced with permission from *Europhys. Lett.*, 1995, **29**, 469.)

function of the film coverage is used to show that the changes in the electronic structure as a function of Mg density can be understood in a Mott-Hubbard model, rather than as a simple Wilson transition as might be expected for divalent metal films.¹⁵

Defect-induced Surface Transitions: $\text{K}_{0.3}\text{MoO}_3$

An unusual metal to non-metal transition that has been discovered using photoemission spectroscopy occurs at the surface of the quasi-1D conductor $\text{K}_{0.3}\text{MoO}_3$.^{62,63,86} This material was described in detail in Section 4 in the context of bulk studies of the Peierls transition. However, it has been found that certain defects at the surface of this oxide can produce a dramatic metal to non-metal transition. This discovery was the result of the extreme sensitivity of the surface to electron, ion, and photon beam damage. The issue of defects was discussed briefly in Section 4 in the context of modification of the photoemission intensity near E_F . This topic is developed more fully here.

Fig. 34 shows a series of normal emission ARP spectra taken at room temperature with 18 eV photons from $\text{K}_{0.3}\text{MoO}_3$, and they reveal a dramatic metal to non-metal transition at the surface as a function of defect density.^{62,86} The samples were cleaved in UHV and an SDA-type analyser with 75 meV resolution was used. Spectrum (a) is that of the cleaved surface, and the feature close to E_F is emission from the Mo 4d states. The sensitivity of the surface to a very low density of defects is evident from inspection of spectrum (b), which shows the normal emission spectrum following 4 min of bombardment of the surface with 500 eV Ne^+ ions. For this low density of defects, the

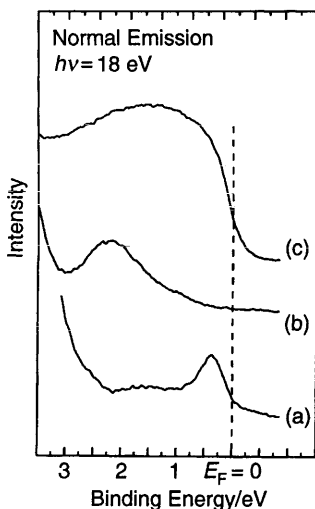


Fig. 34 ARP normal emission spectra from $K_{0.3}MoO_3$; $h\nu = 18$ eV. (a) Cleaved; (b) after 4 min of sputtering with 500 eV Ne^+ ions; (c) after 52 min sputtering. (Reproduced with permission from *J. Phys. Chem. Solids*, 1996, in the press and *J. Vac. Sci. Technol.*, 1994, **12**, 2196.)

Mo 4d emission at E_F completely disappears, and a discrete defect peak develops at 2 eV below E_F , which is within a bulk band gap between the O 2p and Mo 4d bands. Fig. 34(c) shows the result of continued ion bombardment.^{62,66} It is clear that for a high density of defects, the intensity of the emission from the defect state increases and broadens, shifts towards E_F , and produces a large increase in the emission intensity at E_F . The sputtering of the surface is accompanied by a strong increase (0.9 eV) of the work function (Φ) for low defect density surfaces, followed by a gradual, but equally large decrease as the density of defects increases.⁶² The basic electronic structure of defects on surfaces of $K_{0.3}MoO_3$ has been discussed in ref. 62 and 63, and the ARP and work function data are interpreted as revealing a sequential removal of K and O from the surface with ion bombardment.

As regards identification of the defect leading to a state at 2 eV in the bulk band gap, resonant photoemission and photon stimulated desorption (PSD) have been used to determine that this defect is an oxygen vacancy.^{62,63} In PSD, a transition metal oxide is exposed to photons with energy greater than the optical absorption edge of a transition metal core level. If there is no rapid decay channel for the core hole, an interatomic Auger event will occur, leaving the oxygen atom in a doubly positive state which causes the O atoms to be repelled out of the lattice.⁸⁷ Note that PSD leads to O vacancies in the surface layer only. $K_{0.3}MoO_3$ is found to be highly sensitive to PSD damage, and such damage (*i.e.*, O vacancies in the surface layer) lead to an identical peak at 2 eV in the photoemission spectra. Fig. 35 shows the relative intensity of the emission from the defect state as the photon energy is varied from 30 to 100 eV.⁸⁸ As can be seen there is a sharp resonance in the defect emission intensity at a photon energy of about 50 eV, with

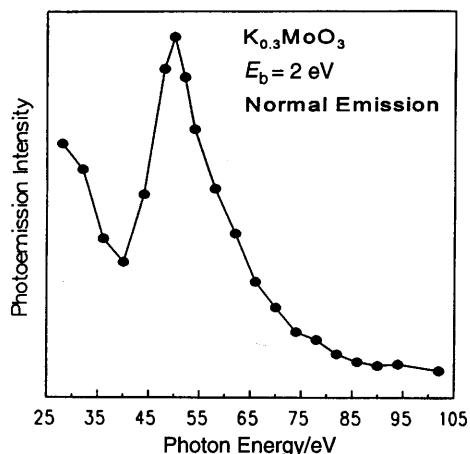


Fig. 35 Resonant photoemission from the 2 eV defect state in $K_{0.3}MoO_3$ revealing the Mo 4d character. The relative intensity of the emission at 2 eV below E_F as a function of incident photon energy is shown. See text for details. (Reproduced with permission from *Solid State Commun.*, 1995, **94**, 601.)

an onset at about 40 eV. The origin of this rapid increase in intensity is Mo 4p \rightarrow 4d resonant photoemission. As described in Theory, as the photon energy is increased through this absorption edge, emission from states with an Mo 4d character is expected to show a dramatic increase in intensity. The observed resonance of the defect state shows that it has Mo 4d character, as expected for an O vacancy.⁸⁸

The defect-induced metal to non-metal transition is also visible in the core level spectra. Fig. 36 presents Mo 3d XPS spectra from (a) a cleaved $K_{0.3}MoO_3$ surface; (b) a low defect density surface; and (c) a high defect density surface. As before, defects were created by 500 eV ion bombardment (although Ar^+ rather than Ne^+ was used). The two primary peaks in the spectra are due to spin-orbit splitting, and correspond to Mo 3d_{5/2} and Mo 3d_{3/2} emission.⁸⁹ The effect of the metal to non-metal transitions at the surface due to defects is quite strong. The spectrum from the low defect density surface shows a shift of the Mo 3d emission towards higher binding energies and a change in line shape. This latter effect is most obvious on the low binding energy side of the emission, where the onset of the Mo 3d line is not as steep as for the cleaved surface. The opposite effect can be seen on the high binding energy side, where the extended tail is absent. For the high defect density surface [Fig. 36(c)] a large shift of the entire Mo 3d emission towards smaller binding energies and a narrowing of the emission features is observed. The measured line shape for the cleaved surface is in agreement with an earlier study by Wertheim *et al.*⁸⁹ where it was shown that the Mo 3d line shape is dominated by final state effects. As was the case for the V 2p emission from V_2O_3 discussed in Section 4, two sets of spin-orbit split doublets are required for a reasonable fit to the data, corresponding to two different screening processes. One mechanism for screening is the transfer of electrons from the valence band to the Mo 4d conduction band; this is the only screening process possible in insulators such as MoO_3 . The

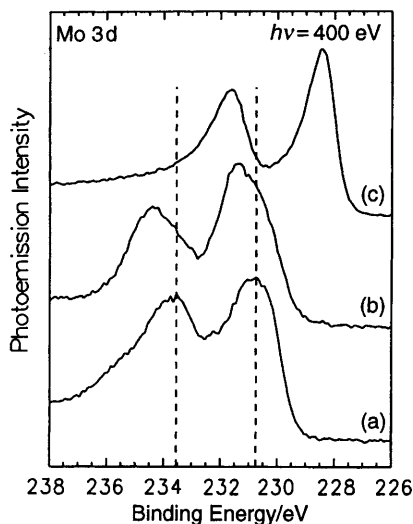


Fig. 36 Mo 3d spectra from $K_{0.3}MoO_3$; $h\nu = 400$ eV. (a) Cleaved; (b) 2 min of 500 eV Ar^+ bombardment; (c) 60 min of 500 eV Ar^+ bombardment.

(Reproduced with permission from *Mater. Res. Soc. Symp. Proc.*, 1995, **375**, 133 and *J. Phys. Chem. Solids*, 1996, in the press.)

second screening process is conventional metallic screening due to the electrons that are already occupying Mo 4d states. Metallic screening produces emission features with lower binding energies (higher kinetic energies) than those associated with unscreened emission. A further characteristic of metallic screening is that the emission will have an asymmetric (Doniach–Sunjic) line shape due to the excitation of electron–hole pairs at E_F .²⁸ These effects were discussed in the section on X-ray photoemission spectroscopy.

In order to estimate the contribution of these two different screening channels for photoemission from $K_{0.3}MoO_3$, the data in Fig. 36 were fitted using two spin–orbit doublets. These two components were obtained from a least-square fit using a convolution of Doniach–Sunjic lines with a Gaussian resolution function. Fig. 37 shows how the Mo 3d emission for the cleaved surface, and the low defect density surface, can be approximated with two components that have different singularity indices and widths, but a common spin–orbit splitting. For the cleaved surface [Fig. 37(a)], a superposition of a broad symmetric component with a Mo $3d_{5/2}$ binding energy of 231.4 eV and a narrower asymmetric line at 230.5 eV gives a good fit to the data. The asymmetric component corresponds to the metallic screening channel and is responsible for the steep increase at the low binding energy side and for the extended emission tail at higher binding energy. These features are missing in the spectrum from the low defect density [Fig. 37(b)] and the fit is dominated by the symmetric component that represents the interatomic screening by electrons in the O 2p band. It is clear that the metallic screening channel is suppressed for the low defect density surface, and that

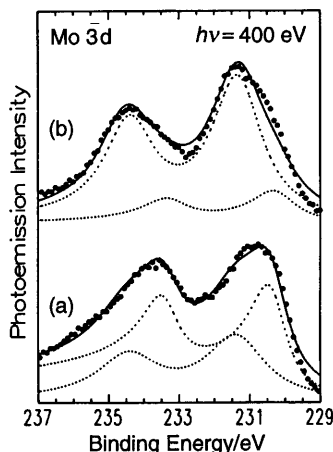


Fig. 37 Mo 3d emission fit with two spin-orbit doublets using a Gaussian resolution function and Doniach-Sunjc line shapes. (a) Cleaved; (b) 2 min of 500 eV Ar^+ bombardment.

(Reproduced with permission from *Mater. Res. Soc. Symp. Proc.*, 1995, **375**, 133 and *J. Phys. Chem. Solids*, 1996, in the press.)

the Mo 3d emission shifts towards higher binding energies. A similar switching on and off of metallic screening is visible in Fig. 9 and 11 for the bulk transition in V_2O_3 . However, while the transition in V_2O_3 can be studied with bulk techniques, this defect-induced transition in $\text{K}_{0.3}\text{MoO}_3$ is a surface effect, for which photoemission spectroscopy is an ideal probe.

Adsorbate Modified Bulk Transitions: $\text{VO}_2 + \text{H}$

The metal to non-metal transitions in V_2O_3 were discussed as the first example in this paper. There is a related transition in the compound VO_2 which has also been studied using photoemission spectroscopy. One fascinating aspect of this transition is the fact that photoemission reveals that it can be inhibited by the adsorption of atomic H on the surface.

For temperatures below 340 K, VO_2 is a semiconductor with a band gap of approximately 0.7 eV and a monoclinic crystal structure.³⁴ Above 340 K, it is a metal with a rutile crystal structure. The change in resistivity is on the order of 10^4 through the transition, and the resistivity as a function of temperature is plotted in Fig. 38.⁹⁰ As with V_2O_3 , the origins of this transition are much debated. The fact that the lattice distorts during the transition could indicate that the resistivity transition is in fact driven by the distortion (due to a change in symmetry of the bands). However, the most commonly ascribed mechanism is that of the Mott transition.⁶

The metal to non-metal transition is clearly visible in angle integrated photoemission spectra from cleaved crystals of VO_2 . (Full details of the surface preparation can be found in ref. 91.) Fig. 39 shows emission from the V 3d states above (351 K) and below (323 K) the transition temperature of 340 K. A CMA was used to obtain the spectra, with light from a synchrotron radiation source. Just as in V_2O_3 , the opening up of the

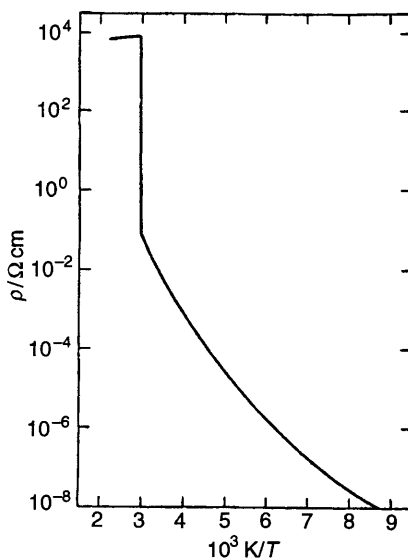


Fig. 38 Resistivity (ρ) as a function of inverse temperature for VO_2 .
(Reproduced with permission from *Solid State Commun.*, 1969, 7, 425.)

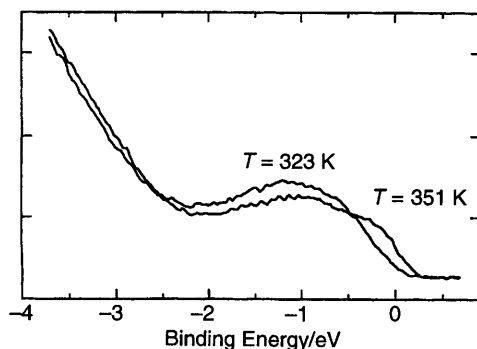


Fig. 39 Angle integrated photoemission spectra from VO_2 above and below the metal to non-metal transition.
(Reproduced with permission from *Phys. Rev. B*, 1992, 45, 9266).

gap is clearly observed, as is the narrowing of the d-band (Section 4). However, if the cleaved surface is exposed to atomic hydrogen, the metal to non-metal transition disappears. Fig. 40 shows a series of angle integrated photoemission spectra for VO_2 : spectrum 1 is that from the cleaved surface at room temperature, spectrum 2 is that following exposure to $1 \times 10^4 \text{ L H}_2^*$, where H_2^* indicates H_2 gas excited by exposure to a naked electron filament in vacuum. Spectra 3 and 4 are those for the modified

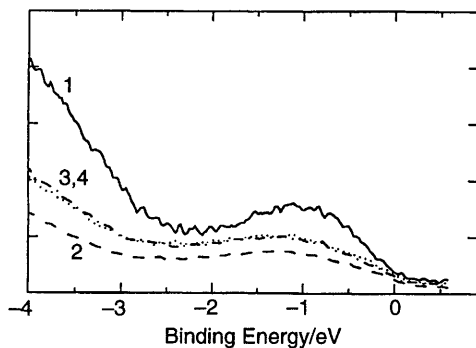
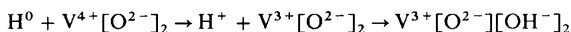


Fig. 40 Series of AIP spectra from VO_2 as a function of exposure of the surface to atomic H. 1, Cleaved surface at room temperature; 2, this surface exposed to $1 \times 10^4 \text{ L H}_2^*$; 3, the exposed surface at 351 K; and 4, the exposed surface at 311 K. (Reproduced with permission from *Phys. Rev. B*, 1992, **45**, 9266.)

material at 351 and 311 K, respectively. Spectra 3 and 4 are essentially indistinguishable, and yet these two temperatures bracket the bulk transition temperature. Examination of the spectra further from E_F (not shown) indicate the presence of OH on the surface, and these results suggest a chemical reduction of the VO_2 surface:



This chemisorption process creates what Bermudez *et al.* describe as a ‘dead-layer’ within which the metal to non-metal transition is suppressed.⁹¹ The creation of this layer is non-reversible: annealing the sample in UHV for 45 min at $\sim 390 \text{ K}$ had no effect. The origin of this suppression is not clear. One possible explanation involves a local relaxation of the surface lattice due to the H adsorption. This would lead to an increased V–O π -bonding interaction, pulling the occupied part of the d-band to higher binding energy and making metallic conduction energetically unfavourable. Not considered in this explanation is the effect of the electrons donated by the adsorbed H atoms into the V 3d states. Experiments such as these could be novel methods of probing electron correlation effects using photoemission spectroscopy.

6 Future Directions

In this paper I have attempted to show that photoemission spectroscopy is a very powerful probe of bulk and surface metal to non-metal transitions. It can provide unique information on the changes in electronic structure during the transitions, and can elucidate the driving mechanisms for the transitions themselves. However, I have also attempted to describe some of the complications that accompany this spectroscopy, and have emphasized the attention that must be paid to surface preparation. The samples presented in this article serve as case studies of the use of photoemission in the

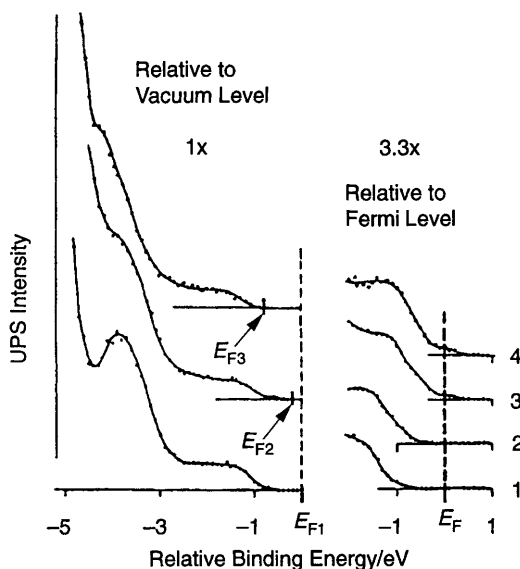


Fig. 41 AIP spectra from thin films of pure and NOPF₆-doped P3HT taken at 233 K with 21.2 eV (He I) photons. 1, Undoped; 2 and 3, intermediate doping; 4, saturated doping.

(Reproduced with permission from *Phys. Rev. Lett.*, 1984, **63**, 1841.)

study of numerous types of metal to non-metal transitions, and it is clear that it is a rich field of research. Furthermore, while photoemission studies of the metal–superconductor transition have been omitted here, they form a large and growing area of research. In this final section I wish to speculate briefly on the future directions of this field.

Four broad new or emerging applications of photoemission spectroscopy in the study of metal to non-metal transitions can be identified: Fermi surface studies, detailed band structure measurements, the study of organic materials, and the use of photoelectron microscopy. The first of these involves the use of very high resolution ARP to measure the Fermi surfaces controlling many metal to non-metal transitions, and also to measure the detailed changes in the Fermi surfaces as any metal to non-metal transition is approached. An example of such studies was presented in Section 4, where measurement of the room temperature Fermi surface of Na_{0.9}Mo₆O₁₇ was discussed. It would be fascinating measure the evolution of this Fermi surface, and such studies could reveal significant new information concerning electron phonon interactions through the transitions. The second new area is related to the Fermi surface studies in that it involves the use of very high resolution ARP to measure the full band dispersion of the states near E_F . Much of the work discussed here involved simply density of states measurements. However, as is clear from the work of Dowben *et al.* for Mg thin films that was discussed in Section 5, the ability to measure the evolution of the full band structure, and hence the ability to measure effective masses, allows a detailed comparison with theory. The third growth area that can be identified is in the use of

photoemission spectroscopy to study organic materials. Much of the work discussed in this paper has been limited to simple inorganic solids. Numerous fascinating metal to non-metal transitions exist in organic and polymer systems, and photoemission spectroscopy can play a significant role in understanding their origins if the problems associated with surfaces in these systems can be solved. One example of such work was discussed in Section 4, where the electronic structure of (DCNQI)₂Cu crystals was under investigation. A further example is provided by a study of a composition induced metal to non-metal transition in thin films of the conjugated polymer P3HT [poly(3-hexylthiophene)] doped with NOPF₆. Fig. 41 shows a series of angle integrated photoemission spectra as a function of dopant concentration.⁹¹ Clear changes in the density of states at E_F are visible as the dopant is introduced into the film. These photoemission data are used to verify a previously unobserved polaron model for the nature of the saturated doped films.^{92,93} Such studies of polymer films, and of organic solids, show that with care photoemission spectroscopy can be successfully applied to these complex systems. Finally, an area of great interest at present is the reduction in the spatial resolution of photoemission analysers. Much progress has been made recently in so-called photoelectron microscopy, where the electronic structure of solids can be probed on a sub-micron length scale.^{94,95} The possibility of using such microscopes to study spatially localized metal to non-metal transitions, or transitions in mesoscopic structures and clusters is quite exciting.

In conclusion, photoemission spectroscopy has proved to be a unique method of studying solid state metal to non-metal transitions, and has contributed much towards our understanding of these transitions. The prospects for the continued development of the spectroscopy, and its continued utility in this area of research are excellent.

Acknowledgements. I would like to thank the following people who have participated in some of the work reported here: (in alphabetical order) Klaus Breuer, David Goldberg, Victor Henrich, Steve Hulbert, Bill McCarroll, and Cristian Stagarescu. I particularly wish to thank Martha Greenblatt for a fruitful collaboration and for numerous illuminating discussions. Finally, Mike Whangbo and Enric Canadell are gratefully acknowledged for their help and advice.

Part of the research reported here was supported by the National Science Foundation under CAREER award DMR 9501174, and by the Petroleum Research Fund, administered by the American Chemical Society. Much of our research was undertaken on the Boston University/North Carolina State University/NSLS beamline U4A at the National Synchrotron Light Source, Brookhaven National Laboratory, which is supported by the US DOE, Divisions of Materials Sciences and Chemical Sciences.

References

- 1 *Photoemission in Solids*, Parts 1 and 2, ed. M. Cardona and L. Ley, Springer Verlag, Berlin, 1978.
- 2 *Angle Resolved Photoemission*, ed. S. D. Kevan, Elsevier, Amsterdam, 1991.
- 3 K. E. Smith and S. D. Kevan, *Prog. Solid State Chem.*, 1991, **21**, 49.
- 4 E. W. Plummer and W. Eberhardt, *Adv. Chem. Phys.*, 1982, **49**, 533.
- 5 Z.-X. Shen and D. S. Dessau, *Phys. Rep.*, 1995, **253**, 1, and references therein.
- 6 N. Mott, *Metal-Insulator Transitions*, Taylor and Francis, London, 1974.
- 7 J. Hubbard, *Proc. R. Soc. London, A*: 1963, **237**, 238; 1964, **281**, 401.

- 8 J. Zaanen, G. A. Sawatzky and J. W. Allen, *Phys. Rev. Lett.*, 1985, **55**, 418.
- 9 P. W. Anderson, *Phys. Rep.*, 1958, **109**, 1492.
- 10 E. Wigner, *Trans. Faraday Soc.*, 1938, **34**, 678.
- 11 P. A. Miles, W. B. Westphal and A. von Hippel, *Rev. Mod. Phys.*, 1957, **29**, 279.
- 12 *Low Dimensional Electronic Properties of Molybdenum Bronzes and Oxides*, ed. C. Schlenker, Kluwer, Dordrecht, 1989.
- 13 *Crystal Chemistry and Properties of Materials with Quasi-One-Dimensional Structures*, ed. J. Rouxel, Reidel, Dordrecht, 1986.
- 14 *Physics and Chemistry of Low Dimensional Inorganic conductors*, ed. C. Schlenker, J. Dumas, M. Greenblatt and S. van Smaalen, NATO ASI Series B: Physics, Plenum, NY, in the press.
- 15 E. W. Plummer and P. A. Dowben, *Prog. Surf. Sci.*, 1993, **42**, 201.
- 16 S. K. Chan and V. Heine, *J. Phys. F*, 1973, **3**, 795.
- 17 W. Kohn, *Phys. Rev. Lett.*, 1959, **2**, 392.
- 18 M.-H. Whangbo, E. Canadell, P. Foury and J.-P. Pouget, *Science (Washington, D.C., 1883—)*, 1991, **252**, 96.
- 19 M.-H. Whangbo, J. Ren, W. Liang, E. Canadell, J.-P. Pouget, S. Ravy, J. M. Williams and M. A. Beno, *Inorg. Chem.*, 1995, **31**, 4169.
- 20 C. Kunz, *Synchrotron Radiation: Techniques and Applications*, Springer, Berlin, 1979; G. Margaritondo, *Introduction to Synchrotron Radiation*, Oxford University Press, New York, 1988; *Handbook of Synchrotron Radiation*, ed. E. Koch, North-Holland, Amsterdam, 1983; *Synchrotron Radiation Research: Advances in Surface Science*, ed. R. Z. Bachrach, Plenum, New York, 1990.
- 21 G. D. Mahan, *Phys. Rev. B*, 1970, **2**, 4334; P. J. Feibelman and D. E. Eastman, *Phys. Rev. B*, 1974, **10**, 4932; J. E. Inglesfield and E. W. Plummer, in *Angle Resolved Photoemission*, ed. S. D. Kevan, Elsevier, Amsterdam, 1991.
- 22 R. H. Williams, G. P. Srivastava and I. T. McGovern, *Rep. Prog. Phys.*, 1980, **43**, 1357.
- 23 F. J. Himpsel, *Adv. Phys.*, 1983, **32**, 1.
- 24 J. Hermanson, *Solid State Commun.*, 1977, **22**, 19.
- 25 J. A. Knapp, F. J. Himpsel and D. E. Eastman, *Phys. Rev. B*, 1979, **19**, 4952.
- 26 J. B. Pendry, *Photoemission and the Electronic Properties of Surfaces*, ed. B. Feuerbacher, B. Fitton and R. F. Willis, Wiley, New York, 1978; D. E. Eastman, J. A. Knapp and F. J. Himpsel, *Phys. Rev. Lett.*, 1978, **41**, 825; P. Thyry, D. Chandesris, J. Lecante, C. Guillot, R. Pinchaux and Y. Petroff, *Phys. Rev. Lett.*, 1979, **43**, 82.
- 27 D. Pines and P. Nozieres, *The Quantum Theory of Liquids*, W. A. Benjamin, Menlo Park, CA, 1966.
- 28 L. C. Davis, *J. Appl. Phys.*, 1986, **59**, R25, and references therein.
- 29 S. Doniach and M. Sunjic, *J. Phys. C*, 1970, **3**, 285.
- 30 J. W. Rabalais, *Principles of Ultraviolet Photoelectron Spectroscopy*, Wiley, New York, 1977; J. A. R. Samson, *Techniques of Vacuum Ultraviolet Spectroscopy*, Wiley, New York, 1967; D. Roy and J. D. Carette, *Electron Spectroscopy for Surface Analysis*, ed. H. Ibach, Springer, Berlin, 1977.
- 31 S. D. Kevan, *Rev. Sci. Instrum.*, 1983, **54**, 1441.
- 32 K. E. Smith and V. E. Henrich, *Phys. Rev. B*, 1994, **50**, 1382.
- 33 H. Kuwamoto, J. M. Honig and J. Appel, *Phys. Rev. B*, 1980, **22**, 2626.
- 34 J. B. Goodenough, *Prog. Solid State Chem.*, 1972, **5**, 145.
- 35 D. B. McWhan, T. M. Rice and J. P. Remeika, *Phys. Rev. Lett.*, 1969, **22**, 887; *Phys. Rev. Lett.*, 1969, **23**, 1384.
- 36 J. Spalek, A. Datta and J. M. Honig, *Phys. Rev. Lett.*, 1987, **59**, 728; *Phys. Rev. B*, 1986, **33**, 4891.
- 37 J. Park, Ph.D. Thesis, The University of Michigan, 1994.
- 38 K. E. Smith and V. E. Henrich, *Phys. Rev. B*, 1988, **38**, 5965.
- 39 K. E. Smith and V. E. Henrich, *Phys. Rev. B*, 1988, **38**, 9571.
- 40 K. E. Smith and V. E. Henrich, *Solid State Commun.*, 1988, **68**, 29.
- 41 S. Shin, S. Suga, M. Taniguchi, M. Fujisawa, H. Kanzaki, A. Fujimori, H. Daimon, Y. Ueda, K. Kosuge and S. Kachi, *Phys. Rev. B*, 1990, **41**, 4993.
- 42 R. L. Kurtz and V. E. Henrich, *Phys. Rev. B*, 1982, **25**, 3563.
- 43 K. E. Smith and V. E. Henrich, *Surf. Sci.*, 1990, **225**, 47.
- 44 R. L. Kurtz and V. E. Henrich, *Phys. Rev. B*, 1983, **28**, 6699.
- 45 D. K. G. de Boer, C. Haas and G. A. Sawtsky, *Phys. Rev. B*, 1984, **29**, 4401.
- 46 B. W. Veal and A. P. Paulikas, *Phys. Rev. B*, 1985, **31**, 5399.
- 47 E. Sachar, *Phys. Rev. B*, 1985, **31**, 4029; *Phys. Rev. B*, 1986, **34**, 5130.
- 48 B. W. Brown and E. Banks, *J. Am. Chem. Soc.*, 1954, **76**, 963; P. Hagenmuller, *Prog. Solid State Chem.*, 1972, **5**, 71.
- 49 N. F. Mott, *Philos. Mag.*, 1977, **35**, 111.
- 50 G. Hollinger, P. Pertosa, J. P. Doumerc, F. J. Himpsel and B. Reihl, *Phys. Rev. B*, 1985, **32**, 1987.
- 51 J. P. Doumerc, J. Marcus, M. Pouchard and P. Hagenmuller, *Mater. Res. Bull.*, 1979, **14**, 201.
- 52 F. H. Potter and R. G. Egdel, *Surf. Sci.*, 1993, **287–288**, 649.
- 53 K. E. Smith, *Ann. Rep. Prog. Chem., Sect. C*, 1993, **90**, 115.
- 54 M. Greenblatt, *Chem. Rev.*, 1988, **88**, 31.
- 55 C. Schlenker and J. Dumas, in *Crystal Chemistry and Properties of Materials with Quasi-One-Dimensional Structures*, ed. J. Rouxel, Reidel, Dordrecht, 1986.

- 56 J. P. Pouget, S. Kagoshima, C. Schlenker and J. Marcus, *J. Phys. Lett.*, 1973, **44**, L113.
- 57 B. Dardel, D. Malterre, M. Grioni, P. Weibel, Y. Baer and F. Lévy, *Phys. Rev. Lett.*, 1991, **67**, 3144.
- 58 B. Dardel, D. Malterre, M. Grioni, P. Weibel, Y. Baer, C. Schlenker and Y. Petroff, *Europhys. Lett.*, 1992, **19**, 525.
- 59 K. Terashima, H. Matsuoka, K. Soda, S. Suga, R. Yamamoto and M. Doyama, *J. Phys. Soc. Jpn*, 1988, **57**, 2557.
- 60 K. Ohtake, H. Matsuoka, R. Yamamoto, M. Doyama, H. Sakamoto, T. Mori, K. Soda and S. Suga, *J. Phys. C*, 1986, **19**, 7207.
- 61 G. K. Wertheim, L. F. Schneemeyer and D. N. E. Buchanan, *Phys. Rev. B*, 1985, **32**, 3568.
- 62 K. Breuer, K. E. Smith, M. Greenblatt and W. McCarroll, *J. Vac. Sci. Technol.*, 1994, **12**, 2196.
- 63 K. E. Smith, K. Breuer, D. M. Goldberg, M. Greenblatt, W. McCarroll and S. L. Hulbert, *Mater. Res. Soc. Symp. Proc.*, 1995, **375**, 133.
- 64 J. M. Luttinger, *J. Math. Phys. (N.Y.)*, 1963, **4**, 1154; S. Tomonaga, *Prog. Theor. Phys.*, 1950, **5**, 349; J. Solyom, *Adv. Phys.*, 1979, **28**, 201; H. J. Schulz, *Int. J. Mod. Phys. B*, 1991, **5**, 57.
- 65 A. Sekiyama, A. Fujimori, S. Aonuma, H. Sawa and R. Kato, *Phys. Rev. B*, 1995, **51**, 13899.
- 66 K. Singzer et al., *J. Am. Chem. Soc.*, 1993, **115**, 7696.
- 67 P. D. Hambourger and F. J. DiSalvo, *Physica B*, 1980, **99**, 173.
- 68 *Physics and Chemistry of Materials with Layered Structures*, ed. F. Lévy, Reidel, Dordrecht, 1976, vol. 1–5.
- 69 A. Wilson, F. J. DiSalvo and S. Mahajan, *Adv. Phys.*, 1975, **24**, 117.
- 70 B. Dardel, M. Grioni, D. Malterre, P. Weibel, Y. Baer and F. Lévy, *Phys. Rev. B*, 1992, **45**, 1462.
- 71 B. Dardel, M. Grioni, D. Malterre, P. Weibel, Y. Baer and F. Lévy, *Phys. Rev. B*, 1992, **46**, 7407.
- 72 N. V. Smith, S. D. Kevan and F. J. DiSalvo, *J. Phys. C*, 1985, **18**, 3175.
- 73 K. Breuer, C. Stagarescu, K. E. Smith, M. Greenblatt and K. Ramanujachary, *Phys. Rev. Lett.*, 1996, **76**, 3172.
- 74 M.-H. Whangbo, E. Canadell and C. Schlenker, *J. Am. Chem. Soc.*, 1995, **109**, 6308.
- 75 C. Escribe-Filippini, K. Konate, J. Marcus, C. Schlenker, R. Almairac, R. Ayroles and C. Rouacau, *Philos. Mag.*, 1984, **B50**, 321.
- 76 A. Chainani, T. Yokoya, T. Morimoto, T. Takahashi and S. Todo, *Phys. Rev. B*, 1995, **51**, 976.
- 77 R. J. Lad and V. E. Henrich, *Phys. Rev. B*, 1994, **39**, 1989.
- 78 S. F. Alvarado et al., *Phys. Rev. Lett.*, 1975, **34**, 319.
- 79 V. E. Henrich, *Rep. Prog. Phys.*, 1985, **48**, 1481.
- 80 J. H. Park, L. H. Tjeng, J. W. Allen, P. Metcalf and C. T. Chen, *Phys. Rev. Lett.*, 1996, submitted for publication.
- 81 E. W. Plummer, J. M. Carpinelli, H. H. Weitering and P. A. Dowben, *Phys. Low Dim. Struct.*, 1994, **4–5**, 99.
- 82 P. A. Dowben, D. N. McIlroy, J. Zhang and E. Ruhl, *Mat. Sci. Eng.*, 1996, in the press.
- 83 J. Zhang, D. N. McIlroy and P. A. Dowben, *Europhys. Lett.*, 1995, **29**, 469.
- 84 J. Zhang, D. N. McIlroy and P. A. Dowben, *Phys. Rev. B*, 1994, **49**, 780.
- 85 J. Zhang, D. N. McIlroy and P. A. Dowben, *Phys. Rev. B*, 1994, **52**, 380.
- 86 K. Breuer, K. E. Smith, M. Greenblatt, W. McCarroll and S. L. Hulbert, *J. Phys. Chem. Solids*, 1996, in the press.
- 87 M. L. Knotek and P. J. Feibelman, *Phys. Rev. Lett.*, 1978, **40**, 964.
- 88 K. Breuer, D. M. Goldberg, K. E. Smith, M. Greenblatt and W. McCarroll, *Solid State Commun.*, 1995, **94**, 601.
- 89 G. K. Wertheim, L. F. Schneemeyer and D. N. E. Buchanan, *Phys. Rev. B*, 1985, **32**, 3568.
- 90 L. A. Ladd and W. Paul, *Solid State Commun.*, 1969, **7**, 425.
- 91 V. M. Bermudez, R. T. Williams, J. P. Long, R. K. Reed, P. H. Klein, *Phys. Rev. B*, 1992, **45**, 9266.
- 92 M. Lögdung, R. Lazzaroni, S. Stafström, W. R. Salaneck and J.-L. Brédas, *Phys. Rev. Lett.*, 1989, **63**, 1841.
- 93 S. Stafström and J.-L. Brédas, *Phys. Rev. B*, 1988, **38**, 4180.
- 94 S. Kivelson and A. J. Heeger, *Phys. Rev. Lett.*, 1985, **55**, 308.
- 95 H. Ade, *Nucl. Instrum. Methods Phys. Res., Sect. A*, 1992, **319**, 311.
- 96 *Chemical, Structural and Electronic Analysis of Heterogeneous Surfaces on Nanometer Scale*, R. Rossei, ed., Kluwer, Dordrecht, 1996, in the press.